Hydrodynamic simulations with a radiative surface

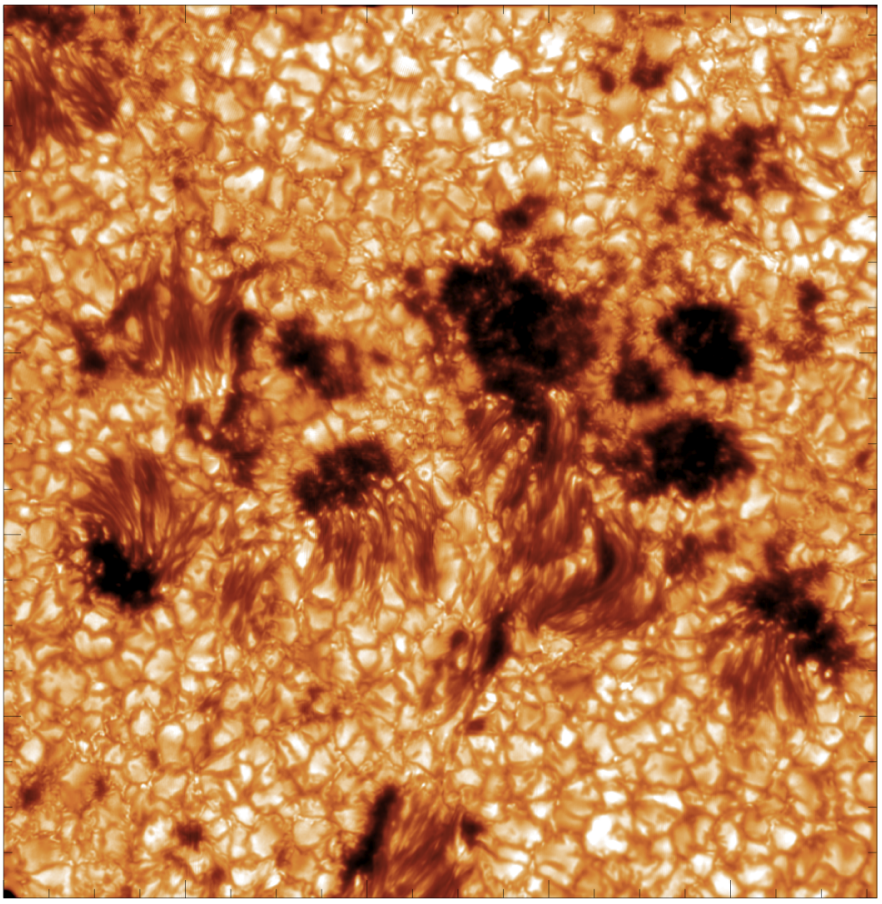

Atefeh Barekat
Department of Astronomy, Stockholm University, Sweden
Nordita, KTH Royal Institute of Technology and Stockholm University, Sweden

Image of a sunspot (AR1589). Observed with CRISP at the Solar Swedish Telescope (SST) on La Palma, Spain at a wavelength of 557.6 nm on 15th of October 2012. Observation by Atefeh Barekat and data reduction by Mats Löfdahl, Jörn Warnecke and Atefeh Barekat.

Department of Astronomy

Nordita

Hydrodynamic simulations with a radiative surface

Master Thesis

Atefeh Barekat

May 27, 2013

Supervisor
Axel Brandenburg

Contents

Abstract

We solve the equations of radiation hydrodynamics to compute the time evolution toward one-dimensional equilibrium solutions using a generalized Kramers opacity, $\kappa = \kappa_0 \rho^a T^b$, with adjustable prefactor κ_0 and exponents a and b on density ρ and temperature T, respectively. We choose our initial conditions to be isothermal and find that the early time evolution away from the isothermal state is fastest near the height where the optical depth is unity, and is slower both above and below it. In all cases where the quantity $n = (3-b)/(1+a)$ is larger than -1, we find a nearly polytropic solution with $\rho \propto T^n$ in the lower part and a nearly isothermal solution in the upper part with a radiating surface in between, where the optical depth is unity. In the lower part, the radiative diffusivity is found to be approximately constant, while in the upper optically thin part it increases linearly. Interestingly, solutions with different parameter combinations a and b that result in the same value of n are rather similar, but not identical. Increasing the prefactor increases the temperature contrast and lowers the value of the effective temperature. We find that the Péclet number based on sound speed and pressure scale height exceeds numerically manageable values of around 10^4 when the prefactor κ_0 is chosen to be approximately six orders of magnitude below the physically correct value. In the special case where $a = -1$ and $b = 3$, the value of n is undetermined and the radiative diffusivity is strictly constant everywhere. In that case we find a stratification that is approximately adiabatic. Finally, exploratory two-dimensional calculations are presented where we include turbulent values of viscosity and diffusivity and find that onset of convection occurs when these values are around $3 \times 10^{13}\,\mathrm{cm^2\,s^{-1}}$. The addition of an imposed horizontal magnetic field suppresses small-scale convection, but has not led to instability in the cases investigated so far.

Chapter 1

Introduction

1.1 The Sun

The distance of the Sun to the Earth is just $R_{\mathrm{E}\odot} \approx 8$ light minutes, compared to 4 light years to our nearest star alpha Centauri. This vicinity and the existence of advanced observing techniques provide a great opportunity for studying this star in more detail than any other star. Hence, we posses precise measurement of solar parameters such as luminosity $L_\odot$, radius $R_\odot$ and mass $M_\odot$ (see Table 1.1). By knowing the general physical properties of the Sun we can also derive some other useful quantities such as the effective temperature T_{eff} and the gravitational acceleration on the surface g,

$$T_{\mathrm{eff}} = \left(\frac{L_\odot}{4\pi R_{\mathrm{E}\odot}^2 \sigma_{\mathrm{SB}}} \right)^{1/4} = 5780\,\mathrm{K}, \tag{1.1}$$

$$g = \frac{GM_\odot}{R_\odot^2} \approx 2.74 \times 10^4\ \mathrm{cm\,s^{-2}}, \tag{1.2}$$

where G is Newton's gravitational constant and σ_{SB} is the Stefan-Boltzmann constant (see Table 5.1 for an overview of universal constants). It is common to split the Sun into two parts: the solar *interior* and the solar *atmosphere*. The interior can be divided into three parts itself (see Figure 1.1):

1. The core, $0 < R_{\mathrm{cor}} \leq 0.3\,R_\odot$.
2. The radiative zone, $0.3\,R_\odot \leq R_{\mathrm{rad}} \leq 0.7\,R_\odot$.
3. The convection zone, $0.7\,R_\odot \leq R_{\mathrm{con}} \leq 1\,R_\odot$.

In the core, where the temperature is $T_c \approx 1.6 \times 10^7$ K, hydrogen is burned to helium providing the main energy of the Sun. The released energy is transported via radiation in the *radiation zone*. In this highly dense region, the photons perform a random walk to transport this energy. It takes around 50,000 years that a photon which is produced in the core, can reach the surface and escape. The outer-most interior part of the Sun is the *convection zone* where the energy is transported via convection. We can only see the surface of the convection zone. Herschel (1801) was the first who observed the pattern of the surface of the convection zone called granulation. He described it as some "hot clouds" passing through the cooler overlying atmosphere above the surface of the Sun (Nordlund et al., 2009). The horizontal size of each granule is around 1 Mm. In these cells the hot plasma

Table 1.1: Solar parameters (Stix, 1989).

parameter	SI	cgs
Distance ($R_{E\odot}$)	1.5×10^{11} m	1.5×10^{13} cm
Mass ($M_\odot$)	10^{30} kg	10^{33} gr
Radius ($R_\odot$)	$7{\times}10^{8}$ m	$7{\times}10^{10}$ cm
Luminosity ($L_\odot$)	4×10^{26} W	4×10^{33} erg

rises in the middle and sinks down at their boundaries, the intergranular lanes. Although, we cannot observe the interior of the Sun directly, there is an advanced technique named *helioseismology* that gives insight about some properties of the interior of the Sun. In this technique oscillatory acoustic waves are used to gain information such as temperature and velocities as the differential rotation of the interior of the Sun. For instance, we have an independent verification of the depth of the convection zone from this technique which has thus important impact on constructing a realistic solar model. In the convection zone, the temperature varies from 4500 K to 6000 K near the top to about 2×10^6 K at the bottom.

Above the convection zone, there is the atmosphere of the Sun which again consists of three different parts: photosphere, chromosphere and corona. The photosphere is a thin layer with $\approx$ 500 km depth where the surface of the Sun is located. The Sun does not have a sharp surface. By definition, the surface of the Sun is where the optical depth (see Section 2.6.3) of the continuum of the line $\lambda = 500$ nm is equal to unity ($\tau_{500} = 1$). In the photosphere the temperature varies from 4500 K to 6000 K. The dominant continuum opacity near the photosphere is due to the continuum line $\lambda = 1645$ nm, which corresponds to the ionization energy of H^-. Understanding the properties of the photosphere plays an important role for our knowledge about the structure of the Sun. This is due to the fact that the energy carried by convection can be radiated away in the photosphere. The chromosphere lies on top of the photosphere and is about 2 Mm deep. As we go outward from the bottom of the chromosphere to the surrounding medium, the temperature increases to about 35000 K, but the density decreases. This layer is visible during the solar eclipse. We can observe emission lines of helium due to the temperature increase in this layer. Above the chromosphere is the corona which has a low density but a high temperature up to 10^6 K. The origin of this high temperature is known as the *corona heating problem*, because the corona needs an additional heat source to maintain these high temperature. It is regarded as an unsolved problem in solar physics (but see Gudiksen & Nordlund, 2005, for a realistic model that seems to have solved this problem). One of the most important features of solar variability is its magnetic field. For example in many phenomena on the solar surface such as sunspots, the magnetic field plays a crucial role. However, we were not aware of the existence of the magnetic field in the Sun until the beginning of the 20th century when Hale (1908) studied the solar spectral lines in sunspots and found signatures

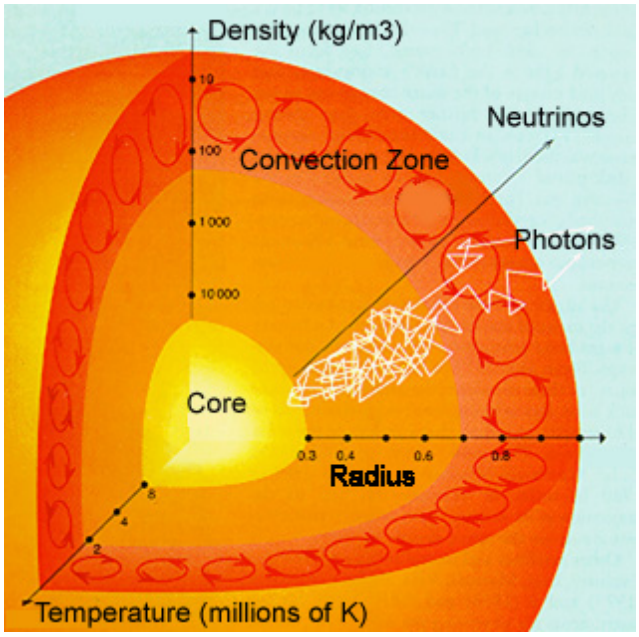

Figure 1.1: The interior of the Sun. The yellow, orange and red color represents the core, the radiation zone and the convection zone, respectively. A white line shows the random walk path of photons that created in the core and reach to the surface and a black line shows neutrinos that is created due to the fusion in the core and can escape directly without any interaction with the matter. The picture is taken from UCB's Center for Science Education.

of Zeeman splitting[1]. It was the first time it was found that a celestial object can contain magnetic fields. The magnetic field of the Sun is believed to be generated by a dynamo mechanism in the convection zone. The Sun has an oscillating magnetic field which changes locally and globally over time. The global magnetic field shows a cyclic behavior of 22 years on average. This cycle is correlate with the 11 years cycled based on the appearance and evolution of the sunspots on the surface of the Sun. In the beginning of the cycle, sunspots appear at latitudes between 20° and 30°. At the end of the cycle, sunspots appear close to the equator. The number of sunspots changes during the cycle. At sunspot maximum, there can exist a few hundred spots per month and at sunspot minimum, a few or even no sunspots during an entire year. There is no clear explanation about the cyclic behavior of the global magnetic field of the Sun. This is one of the main interests of solar physics. Our knowledge about the magnetic field of the Sun is not complete yet, but we know that the magnetic field is an omnipresent part of the Sun and it is dynamic. This is due to the fact that the Sun is made of plasma. This plasma is highly conducting, causing the fluid plasma to carry the magnetic field along.

[1]The Zeeman splitting is the effect of the magnetic field on the spectral line which splits the line into several components.

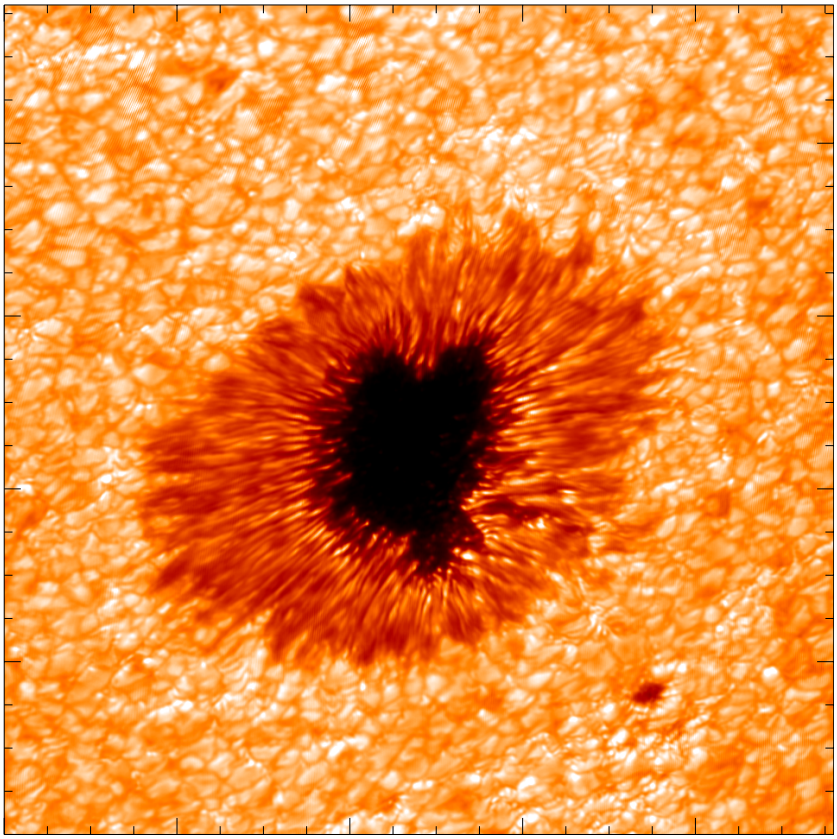

Figure 1.2: Image of a sunspot (AR1591). Observed with CRISP at the Solar Swedish Telescope (SST) on La Palma, Spain at a wavelength of 557.6 nm on 14th of October 2012. Observation by Atefeh Barekat and data reduction by Mats Löfdahl, Jörn Warnecke and Atefeh Barekat.

1.2 Sunspots

Sunspots are dark spots on the surface of the Sun. They consist of two distinguishable parts: *umbra* and *penumbra*. In Figure 1.2 an example of such a sunspot is shown, which has been observed with the Swedish Solar Telescope. The *umbra* is the dark part in the middle of a sunspot. The *penumbra* is the bright filamentary structure around the umbra. The size of sunspots ranges from 10 to 50 Mm. We can observe sunspots with a naked (protected) eye, if they are big enough. Hence, the observation of sunspots has a long history. For a long time sunspots have been considered as planets seen during their transit in front of the Sun. It was in the seventeenth century when Galileo Galilei and contemporaries found sunspots with their telescopes and recognized that they are the features of the Sun itself. It was not clear what they are until the beginning of the twentieth century when Hale (1908) noticed that sunspots are correlated with a magnetic field concentration. Nowadays, we know that the magnetic field of a sunspot is 3000–4000 G. Furthermore, at the surface of the Sun, these features seem to be darker compared to their surrounding granulation, because they

are cooler than the surroundings. The temperature of the umbra can be estimated to be in the range from 3000 to 4000 K. From this important observational information about the correlation of the magnetic field and the temperature, we can conclude that a strong magnetic field can suppress the convective heat transport. This leads to cooling of this area, which then becomes darker compared to the rest of the surface of the Sun. This conjecture was proposed by Biermann in the 1940s and he published his idea in 1941. Since that time, this idea is generally accepted among solar physicists. But the mechanism of sunspot formation is not fully understood yet. There are two main categories of sunspots formation: one category explains the formation processes as a deeply rooted phenomenon and the other one as a near–surface phenomenon. The former conjecture is that the magnetic field is amplified in the interior of the Sun, just below the bottom of the convection zone where the shear is believed to be strong (Schuessler, 1980). This model is called *flux tube model* and it is the standard model of sunspot formation. In this model, in a tube concentrated magnetic field rises from the bottom of the convection zone to the surface and reaches through the photosphere as a bipolar region. We refer the interested reader to the book by Stix (1989) for further discussion. In the second conjecture, the magnetic field is concentrated near the surface of the Sun, rather than deeper in the convection zone. Examples of this category are the paper by Kitchatinov & Mazur (2000), Kemel et al. (2012), and Stein & Nordlund (2012).

1.3 Motivation for the thesis project

In this thesis, we will prepare the ground work for investigating a possibility of the second category of sunspot formation which is based on a turbulent thermo–magnetic instability. The idea is that, when there is an area in the convection zone that contains a magnetic field, this field quenches the convecting heat transport. As a result the fluid plasma around this field becomes cooler, denser and sinks downward. Hence, the warmer plasma close to this area moves toward the cooler region to fill the gap. Magnetic fields which are frozen in this highly conductive plasma, follow the fluid motions. Therefore, more magnetic fields are carried toward the cooler area and lead to field amplification. This instability was investigated by Kitchatinov & Mazur (2000) as an example for sunspot formation. The authors found concentrations of magnetic fields in their simulation by using a quenching of the convective heat transport depending on the magnetic field. They simplify their simulation setup by using a top radiative boundary condition instead of solving the radiative transfer equation. In this thesis, we investigate a similar setup, but include a proper radiative transfer description. We solve radiative transfer because we want to investigate a solar surface phenomenon and we know that radiation at the surface becomes an important mechanism for transporting the heat. Investigating the concentration of magnetic fields in the presence of radiative transfer can be an important step toward improving our understanding of sunspot formation. If we find this instability, it would be a strong indication that sunspot formation can be a near–surface phenomenon instead of a deeply rooted one. Solving the radiative transfer equation in hydrodynamical simulations of solar convection has been done before (see, e.g., Nordlund, 1982; Steffen et al., 1989; Edwards, 1990; Stein & Nordlund, 1998; Vögler et al., 2005). Here we follow the more idealized approach of

Table 1.2: Parameters of the solar convection zone (CZ) at the bottom and near the surface. u, ρ, Re and Re_M are the velocity, density and fluid and magnetic Reynolds number, respectively (Stix, 1989).

	u [m s^{-1}]	ρ [kg m^{-3}]	T[K]	L[m]	Re	Re_M
Bottom CZ	10	10^2	10^6	10^8	10^{13}	10^9
near surface CZ	10^3	10^{-3}	10^4	10^6	10^{12}	10^6

Edwards (1990) in that the *Kramers opacity* (see Section 2.6.2) was used, although here we do not use the *Eddington approximation* to solve the radiative transfer equation.

Realistic simulations of the solar convection zone are not trivial. Including all the dynamics of the whole solar convection zone is difficult with present computations. Both the magnetic and fluid Reynolds numbers (see Section 2.1 and Table 1.2) and the Rayleigh number (see Section 2.5.1) are too high for realistic simulations. In this thesis, we use and solve the *mean-field* equations of magnetohydrodynamics to model our problem in a more realistic fashion. Our goal is to capture the effects of the small-scale dynamics of the convection zone through turbulent transport coefficients and to model it in terms of large-scale quantities. We will explain the basics of the mean–field model in Section 2.5.3. Solving the mean-field equations instead of solving the original equations will allow us use solar-like parameters such as density and gravity for example. More importantly, we can study the interaction of small-scale fluid motions with the magnetic field and we can compare it with analytical theory. Another important issue for doing this simulation properly is knowing the properties of the radiative atmosphere which can have crucial impact on our result. As a prerequisite for our project, which actually is the larger part of the thesis, we run 1D simulations of a radiative gray atmosphere to study the transition from the convection zone (nearly polytropic) to the surface (nearly isothermal) within the domain.

Chapter 2

Framework

2.1 Hydrodynamics

Many astrophysical bodies like stars and galaxies are made of gas. We can then use fluid dynamic equations to pursue the evolution of astronomical systems. This requires (Charbonneau, 2013)

$$\lambda_{\rm mfp} \ll l \ll L, \tag{2.1}$$

where L is the size of the object under study, $\lambda_{\rm mfp}$ is a mean free path of the fluid particles, and l is the typical length scale of the hydrodynamic equations. A fluid is described by its velocity field $\boldsymbol{u}(\boldsymbol{x},t)$ and two independent thermodynamical variables, pressure $p(\boldsymbol{x},t)$ and density $\rho(\boldsymbol{x},t)$. We can study a fluid in two different approaches called *Eulerian* and *Lagrangian*. In the Eulerian approach we study the fluid at a fixed point in space and can investigate how the fluid changes over time $\partial f/\partial t$, where f is a fluid variable. In the Lagrangian approach, we follow the fluid element as it moves with the fluid. Hence, the spatial change of the fluid is given by

$$\frac{\mathrm{D}f}{\mathrm{D}t} = \frac{\partial f}{\partial t} + \frac{\partial f}{\partial x}\frac{\partial x}{\partial t} + \frac{\partial f}{\partial y}\frac{\partial y}{\partial t} + \frac{\partial f}{\partial z}\frac{\partial z}{\partial t} \tag{2.2}$$

$$= \frac{\partial f}{\partial t} + \boldsymbol{u}\cdot\boldsymbol{\nabla} f, \tag{2.3}$$

where $\mathrm{D}/\mathrm{D}t$ is called *advective derivative*. There are two main equations in fluid dynamics. The first one is the continuity equation which comes from the conservation of mass,

$$\frac{\partial \rho}{\partial t} + \boldsymbol{\nabla}\cdot(\rho\boldsymbol{u}) = 0. \tag{2.4}$$

The second one is the momentum equation which comes from the conservation of momentum,

$$\rho\frac{\partial \boldsymbol{u}}{\partial t} + \rho\boldsymbol{u}\cdot\boldsymbol{\nabla}\boldsymbol{u} = -\boldsymbol{\nabla}p + \rho\boldsymbol{\nabla}\Phi + \boldsymbol{F}_{\rm visc} + \boldsymbol{F}, \tag{2.5}$$

where Φ is a gravitational potential, $\boldsymbol{F}$ can be additional external forces such as the Lorentz force for example, and $\boldsymbol{F}_{\rm visc}$ is the viscous force,

$$\boldsymbol{F}_{\rm visc} = \boldsymbol{\nabla}\cdot 2\nu\rho\mathsf{S}, \tag{2.6}$$

where ν is a kinematic viscosity and S is the (traceless) rate of strain tensor

$$\mathsf{S}_{ij} = \frac{1}{2}(u_{i,j} + u_{j,i} - \frac{2}{3}\delta_{ij}u_{k,k}). \tag{2.7}$$

Equation (2.5) is known as the *Navier-Stokes* equation.

Reynolds number

One of the important tools in fluid dynamics that help us to have some insights about the fluid problem is dimensionless parameters. The *Reynolds number* Re is one such parameter and is defined as

$$\mathrm{Re} = \frac{[\text{advection}]}{[\text{dissipation}]} \approx \frac{UL}{\nu}, \tag{2.8}$$

where U and L are typical velocity and length scales of the system. This number can quantify whether a flow is turbulent or laminar. Large Reynolds numbers mean that, in Equation (2.5), the nonlinear term $\rho(\boldsymbol{u}\cdot\boldsymbol{\nabla})\boldsymbol{u}$ dominates over the dissipation term, $\boldsymbol{\nabla}\cdot 2\nu\rho\mathsf{S}$ and the fluid becomes turbulent.

2.2 Magnetohydrodynamics

The Sun is made of plasma that contains charged particles and their motion can create a current density,

$$\boldsymbol{J} = \rho_\mathrm{e}\boldsymbol{u}_\mathrm{e}, \tag{2.9}$$

where ρ_e is the density of charged particles and $\boldsymbol{u}_\mathrm{e}$ is the velocity of the drifting particles. An electric current implies a magnetic field $\boldsymbol{B}$, and the two yield a Lorentz force. Hence, in the presence of a magnetic field there is an extra force that acts on the fluid. In this case, $\boldsymbol{F}$ in Equation (2.5) becomes

$$\boldsymbol{F}_L = \boldsymbol{J}\times\boldsymbol{B}. \tag{2.10}$$

Under some astrophysical conditions where the magnetic field is very weak, the Lorentz force can be neglected, but in other cases like the Sun, the magnetic field cannot be neglected and plays an important role in the dynamics of the Sun. By adding the Lorentz force to the fluid equations, we have two more unknowns. In order to solve the fluid equations, we can use Ohm's law and the Maxwell equations to calculate $\boldsymbol{J}$ based on known quantities and also derive an extra equation for the magnetic field called the *induction equation*. The Maxwell equations are

$$\boldsymbol{\nabla}\times\boldsymbol{E} = -\frac{\partial\boldsymbol{B}}{\partial t} \qquad \text{(Faraday's law)}, \tag{2.11}$$

$$\boldsymbol{\nabla}\times\boldsymbol{B} = \mu_0\boldsymbol{J} + \mu_0\epsilon_0\frac{\partial\boldsymbol{E}}{\partial t} \qquad \text{(Ampere's law)}, \tag{2.12}$$

$$\boldsymbol{\nabla}\cdot\boldsymbol{E} = \frac{\rho_\mathrm{e}}{\epsilon_0}, \qquad \boldsymbol{\nabla}\cdot\boldsymbol{B} = 0 \qquad \text{(Gauss's law)}, \tag{2.13}$$

where $\boldsymbol{E}$ is the electric field, μ_0 is the magnetic permeability, ϵ_0 is permittivity, and $\partial\boldsymbol{E}/\partial t$ is the displacement current which can be neglected in a nonrelativistic medium of sufficient conductivity. Equation (2.12) then reads

$$\boldsymbol{J} = \frac{1}{\mu_0}\boldsymbol{\nabla}\times\boldsymbol{B}. \tag{2.14}$$

In a comoving frame, the *Ohm's law* of charged particles is given by

$$\boldsymbol{J} = \sigma(\boldsymbol{E} + \boldsymbol{u} \times \boldsymbol{B}), \tag{2.15}$$

where σ is the electrical conductivity. We can derive the induction equation by using Equations (2.11) and (2.15)

$$\frac{\partial \boldsymbol{B}}{\partial t} = \boldsymbol{\nabla} \times \left(\boldsymbol{u} \times \boldsymbol{B} - \frac{\boldsymbol{J}}{\sigma} \right) \tag{2.16}$$

If we substitute Equation (2.14) into Equation (2.16) and use Equation (2.13), we can then rewrite the induction equation as

$$\frac{\partial \boldsymbol{B}}{\partial t} = \boldsymbol{\nabla} \times (\boldsymbol{u} \times \boldsymbol{B}) + \eta \nabla^2 \boldsymbol{B} \tag{2.17}$$

where $\eta = 1/\sigma\mu_0$ is a magnetic diffusivity and is assumed to be constant in space. It is useful to write the induction equation based on the vector potential $\boldsymbol{B} = \boldsymbol{\nabla} \times \boldsymbol{A}$ with vanishing electrostatic potential (Weyl gauge)

$$\frac{\partial \boldsymbol{A}}{\partial t} = \boldsymbol{u} \times \boldsymbol{B} + \eta \nabla^2 \boldsymbol{A}. \tag{2.18}$$

In summery, the set of magnetohydrodynamic (MHD) equations is

$$\begin{aligned}
\frac{\partial \rho}{\partial t} + \boldsymbol{\nabla} \cdot (\rho \boldsymbol{u}) &= 0, && (2.19)\\
\rho \frac{\partial \boldsymbol{u}}{\partial t} + \rho \boldsymbol{u} \cdot \boldsymbol{\nabla} \boldsymbol{u} &= -\boldsymbol{\nabla} p + \rho \boldsymbol{\nabla} \Phi + \boldsymbol{F}_{\text{visc}} + \boldsymbol{J} \times \boldsymbol{B}, && (2.20)\\
\frac{\partial \boldsymbol{A}}{\partial t} &= \boldsymbol{u} \times \boldsymbol{B} + \eta \nabla^2 \boldsymbol{A}, && (2.21)\\
\boldsymbol{J} &= \frac{1}{\mu_0} \boldsymbol{\nabla} \times \boldsymbol{B}, \qquad \boldsymbol{B} = \boldsymbol{\nabla} \times \boldsymbol{A} && (2.22)
\end{aligned}$$

and an equation of state which gives the relation between pressure, density and temperature, which will be explained in Section 2.4.

Magnetic Reynolds number

Similar to Re we introduce the *magnetic Reynolds number* Re_M, which is defined as

$$\mathrm{Re}_M = \frac{UL}{\eta}, \tag{2.23}$$

where U and L are respectively the velocity and its length scale variation of the magnetic field in space. For large Re_M, the diffusion term can be neglected, except on small length scales when magnetic diffusion is always important.

2.3 Energy equation

First, we define the specific enthalpy h and relate it to specific heat at constant pressure c_p and specific heat at constant volume c_v,

$$h = e + pv, \tag{2.24}$$

$$c_\mathrm{p} = \left.\frac{dh}{dT}\right|_p, \tag{2.25}$$

$$c_\mathrm{v} = \left.\frac{de}{dT}\right|_v, \tag{2.26}$$

$$c_\mathrm{p} - c_\mathrm{v} = \frac{\mathcal{R}}{\mu}, \tag{2.27}$$

where e is the specific energy and $v = 1/\rho$ is the specific volume. The specific entropy is defined via

$$Tds = de + pdv. \tag{2.28}$$

This we can rewrite it as

$$s/c_\mathrm{p} = \frac{1}{\gamma}\ln p - \ln\rho + s_0, \tag{2.29}$$

where s_0 is an integration constant. The energy equation can be written in terms of the entropy evolution as

$$\rho T\frac{\mathrm{D}s}{\mathrm{D}t} = 2\nu\rho\mathsf{S}^2 + \boldsymbol{\nabla}\cdot\boldsymbol{F}_\mathrm{rad}, \tag{2.30}$$

where $\boldsymbol{F}_\mathrm{rad}$ is the radiative heat flux, discuss in detail in Section 2.6.

2.4 Polytropic approximation

Hydrostatic equilibrium in fluid dynamics means that the pressure p at any point in a fluid at rest is just caused by the weight of the fluid, i.e.

$$\boldsymbol{\nabla}p = \rho\boldsymbol{g}, \tag{2.31}$$

where $\boldsymbol{g} = -\boldsymbol{\nabla}\Phi$ is the gravitational acceleration and ρ is the density. For an ideal gas, the relation of pressure, density, and temperature T is given by the following equation of state

$$p = \frac{\rho\mathcal{R}T}{\mu}, \tag{2.32}$$

where $\mathcal{R}$ is the universal gas constant and μ is the mean molecular weight. In order to solve Equation (2.31), we need to have an extra relation between p, ρ and T to fix the relation between the pressure and the other two variables. To solve the vertical stratification, a common assumption is a power-law relation between pressure and density,

$$p(z) = \tilde{K}\rho(z)^\Gamma, \tag{2.33}$$

where Γ is related to the polytropic index n via $\Gamma = 1 + \frac{1}{n}$ and we assume $\tilde{K}$ to be a constant[1]. Indeed, equation (2.33) is the equation for a polytropic atmosphere, and we can investigate how density and temperature change.

2.4.1 Density stratification

By using both (2.32) and (2.33), we find that density stratification is given by

$$\rho(z) \propto T(z)^n \tag{2.34}$$

where $n = \frac{1}{\Gamma - 1}$. This simple relation carries many useful information. It is worthwhile to explore in more detail this relation to find out what kind of stratification to expect by choosing different values for the polytropic index. For example, one of the interesting questions is whether convection happens in a star or not. This will be discussed in Section 2.5.1.

2.4.2 Temperature stratification

We assume $s_0 = 0$. The adiabatic index γ is defined as $c_\mathrm{p}/c_\mathrm{v}$. By using Equations (2.24) and (2.28), the gradient of pressure reads

$$\frac{1}{\rho}\boldsymbol{\nabla} p = \boldsymbol{\nabla} h - T\boldsymbol{\nabla} s. \tag{2.35}$$

In a polytropic atmosphere, if we assume that the specific entropy s (the entropy per unit mass) is constant over height, we can see that the temperature is proportional to the gravitational potential.

We assume that c_v, c_p, $\tilde{K}$, and s are constants, substitute Equation (2.35) into (2.31), and use (2.25), (2.26), (2.34) and the polytropic relation (2.33), to find the temperature as

$$c_\mathrm{p} T = -\left[\left(1 - \frac{1}{\gamma}\right) \Big/ \left(1 - \frac{1}{\Gamma}\right)\right] \Phi, \tag{2.36}$$

where Φ is the gravitational potential, which is here defined as $\Phi = g(z - z_\infty)$, with $g > 0$ and z_∞ being the height where $\Phi = 0$. In an isentropic[2] atmosphere, s is constant and $\Gamma = \gamma$, so we can write the temperature as

$$T = -\frac{g(z - z_\infty)}{c_\mathrm{p}}. \tag{2.37}$$

As a last remark, the polytropic approximation not only satisfies the hydrostatic equilibrium, but also thermostatic equilibrium (at least in the optically thick approximation, see below). Constant flux of energy fulfills the latter one. For instance, in the thermostatic case, Equation (2.30) shows that, if we assume that the all energy is carried by radiation in a plane-parallel atmosphere, the radiative flux $\boldsymbol{F}_\mathrm{rad}$ satisfies the following equation:

$$\boldsymbol{\nabla} \cdot \boldsymbol{F}_\mathrm{rad} = 0. \tag{2.38}$$

[1] Note that Γ can be different from the adiabatic index γ, γ is related to the thermodynamics (ratio of specific heats), while Γ is related to the stratification.

[2] Isentropic means that all particles of the atmosphere (fluid) have the same value of entropy (Clarke & Carswell, 2007).

In an optically thick medium, $\boldsymbol{F}_{\rm rad}$ can be approximated by

$$\boldsymbol{F}_{\rm rad} = -K\boldsymbol{\nabla}T, \tag{2.39}$$

where K is the radiative heat conductivity. If we assume that K is constant, $\boldsymbol{\nabla}T$ should also stay constant in order to obtain the thermostatic equilibrium. We show that in the polytropic atmosphere the temperature is given by equation (2.37). Therefore the thermostatic equilibrium can be satisfied as follows

$$\boldsymbol{\nabla}\cdot K\boldsymbol{\nabla}T = \boldsymbol{\nabla}\cdot\left[K\boldsymbol{\nabla}(z-z_\infty)\frac{g}{c_{\rm p}}\right] = 0. \tag{2.40}$$

2.5 Convective instability

In the simplest picture of describing convection by an unstable fluid, we assume a small blob of gas with density $\rho_{\rm b}$. We perturb this blob, for instance in the upward direction. If it moves back to its initial position, the fluid is convectively stable but if it continues to rise, it is convectively unstable. There are two main reasonable assumptions that can help us to describe the convective motion. The first one is that the blob does not exchange energy with its surroundings during its rise (or fall); hence it is an adiabatic process. The second one is that the pressure of the blob stays at its surrounding pressure. In other words, the pressure of the blob is balanced with its surroundings by acoustic waves propagation. As a result, $\rho_{\rm b}$ is different from the density of its surroundings $\rho_{\rm s}$. This difference in density leads to an upward buoyancy force when the blob is lighter, $\rho_{\rm b} < \rho_{\rm s}$, i.e., against the direction of gravity $\boldsymbol{g}$, so the force is

$$\boldsymbol{F}_{\rm buoyancy} = (\rho_{\rm b} - \rho_{\rm s})\boldsymbol{g}, \tag{2.41}$$

By using these assumptions, we can find the conditions under which the medium becomes convectively unstable. We investigate the instability criterion in two ways, both of which give the same result. We start by explaining the Schwarzschild criterion and we continue using the entropy equation in the polytropic atmosphere to find the proper polytropic index for which the medium becomes convectively unstable.

2.5.1 Schwarzschild criterion

The blob has been moved from $\tilde{z}_1$ to $\tilde{z}_2$, where $\tilde{z}$ is the *depth* of the atmosphere[3]. In these two points we have

$$p_1 > p_2, \qquad T_1 > T_2, \qquad \tilde{z}_1 > \tilde{z}_2, \qquad \rho_1 > \rho_2 \tag{2.42}$$

According to the two main assumptions, constant pressure and adiabatic exchange of energy of the blob, and the condition above, we expect that the blob expands as it rises to be in pressure balance with its surrounding medium. The buoyancy force can continue acting on the blob if the temperature of the blob stays greater than its surroundings, otherwise the blob becomes denser than its surroundings and falls back. Therefore, in order to find out

[3]The relation between depth and height is $\tilde{z} = -z$.

the condition of instability, we should explore the temperature difference of the blob with its surroundings. The blob has cooled down adiabatically, according to

$$\left(\frac{dT}{d\tilde{z}}\right)_{\rm blob} = \frac{dp}{d\tilde{z}}\left(\frac{dT}{dp}\right)_{\rm ad}, \tag{2.43}$$

where "ad" is the abbreviation of adiabatic. The temperature of the blob at $\tilde{z}_2$ will be then

$$T(\tilde{z}_2)_{\rm blob} = T_1 + \left(\frac{dT}{d\tilde{z}}\right)_{\rm blob}\Delta\tilde{z} \tag{2.44}$$

$$= T_1 + \frac{dp}{d\tilde{z}}\left(\frac{dT}{dp}\right)_{\rm ad}\Delta\tilde{z}. \tag{2.45}$$

The temperature of the medium (med) around the blob at $\tilde{z}_2$ is given by

$$T(\tilde{z}_2)_{\rm med} = T_1 + \frac{dT}{d\tilde{z}}\Delta\tilde{z} \tag{2.46}$$

$$= T_1 + \frac{dp}{d\tilde{z}}\left(\frac{dT}{dp}\right)_{\rm med}\Delta\tilde{z}. \tag{2.47}$$

By subtracting Equation (2.47) from Equation (2.45), we get

$$T(\tilde{z}_2)_{\rm blob} - T(\tilde{z}_2)_{\rm med} = \frac{dp}{d\tilde{z}}\left[\left(\frac{dT}{dp}\right)_{\rm ad} - \left(\frac{dT}{dp}\right)_{\rm med}\right]\Delta\tilde{z}. \tag{2.48}$$

As $\Delta\tilde{z} < 0$ (depth decreases), the only way of satisfying the condition of $T(\tilde{z}_2)_{\rm blob} > T(\tilde{z}_2)_{\rm med}$ is the following

$$\left(\frac{dT}{dp}\right)_{\rm ad} < \left(\frac{dT}{dp}\right)_{\rm med} \qquad \text{(instability)}. \tag{2.49}$$

This condition is known as the *Schwarzschild criterion*. The common form of Equation (2.49) is

$$\left(\frac{d\ln T}{d\ln p}\right)_{\rm ad} < \left(\frac{d\ln T}{d\ln p}\right)_{\rm med} \qquad \text{(instability)}, \tag{2.50}$$

where the double logarithmic temperature gradients are abbreviated by

$$\frac{d\ln T}{d\ln p} = \nabla. \tag{2.51}$$

Therefore, we can write (2.50) as

$$\nabla_{\rm ad} < \nabla \qquad \text{(instability)}. \tag{2.52}$$

In the absence of convection, energy is transported by radiation, hence we can write $\nabla = \nabla_{\rm rad}$, where rad is the abbreviation of radiation. Therefore it is convenient to write the *Schwarzschild criterion* as (see e.g. Bohm-Vitense & Trimble, 1993),

$$\nabla_{\rm ad} < \nabla_{\rm rad} \qquad \text{(instability)}. \tag{2.53}$$

In an adiabatic atmosphere, the pressure is given by $p = \tilde{K}\rho^{\gamma}$. By a simple calculation we find that

$$\nabla_{\rm ad} = \left(\frac{d\ln T}{d\ln p}\right)_{\rm ad} = 1 - \frac{1}{\gamma}. \tag{2.54}$$

Rayleigh number

There is a useful dimensionless parameter which describes the relation between buoyancy and viscosity. This number is called *Rayleigh number*

$$\mathrm{Ra} = \frac{\text{buoyancy}}{\text{viscosity}} = \left(-\frac{1}{c_\mathrm{p}}\frac{\mathrm{d}s}{\mathrm{d}z}\right)_0 \frac{gd^4}{\nu\chi}, \tag{2.55}$$

where s is the specific entropy of the hydrostatic equilibrium solution, d is the distance between the two boundaries, and χ is the radiative diffusivity. In astrophysics, the *Rayleigh number* is generally a large number. The critical *Rayleigh number* $\mathrm{Ra_c}$ is the number at which the dominant energy transfer in the fluid changes from conduction to convection.

2.5.2 Polytropic index criterion

Another way that can helps us to find out whether the fluid is convectively unstable or not is considering the difference of the entropy of the blob with its surroundings. This is due to the fact that the specific entropy of an adiabatic system stays constant. Therefore, the specific entropy of the blob is constant during its rise. If we assume that the atmosphere around the blob is a polytropic one, we can find out under which conditions the atmosphere becomes convectively unstable. We consider a blob of gas that is pushed from $\tilde{z}_1$ with given p_0, T_0, and ρ_0 toward $\tilde{z}_2$ with p, T, and ρ. As in the previous section, we assume that the pressure of interior and exterior of the blob is the same. In a polytropic atmosphere we have

$$\frac{\rho}{\rho_0} = \left(\frac{T}{T_0}\right)^n, \tag{2.56}$$

$$\frac{p}{p_0} = \left(\frac{T}{T_0}\right)^{n+1}, \tag{2.57}$$

$$\frac{T}{T_0} = \frac{\tilde{z}}{H_T}, \tag{2.58}$$

where H_T is the temperature scale height. From the equation of hydrostatic equilibrium it can be shown that

$$H_T = \frac{RT_0}{\mu g}(n+1). \tag{2.59}$$

If we substitute Equations (2.56) and (2.57) into the entropy equation (2.29) and look at the changes of entropy over height we get

$$\frac{1}{c_\mathrm{p}}\frac{\mathrm{d}s}{\mathrm{d}z} = -\frac{1}{c_\mathrm{p}}\frac{\mathrm{d}s}{\mathrm{d}\tilde{z}} = -\frac{n+1}{\gamma\tilde{z}} + \frac{n}{\tilde{z}} = \frac{1}{\tilde{z}}\frac{(\gamma-1)n-1}{\gamma}. \tag{2.60}$$

In order to find the condition under which the blob becomes convectively unstable we should find out the relation of the entropy with density. First, we can use Equation (2.29) and investigate the difference of the entropy of the blob with its surroundings:

$$\Delta s/c_\mathrm{p} = \frac{1}{\gamma}\Delta\ln p - \Delta\ln\rho, \tag{2.61}$$

again with $\Delta \ln p = 0$, as above, $\Delta s = s_i - s_e$, and $\Delta \ln \rho = \Delta(\rho_i - \rho_e)/\rho_i$. There, i stands for interior and e stands for the exterior. In summery, the relation of the entropy and the density can be written as

$$\Delta s = -c_{\rm p}(\Delta \ln \rho). \tag{2.62}$$

We know that s_i stays constant as the blob rises. If s_e decreases with height, the rising blob will find itself in a medium where its density is smaller than its surroundings and the buoyancy force will push it further up and it becomes more unstable. Hence, we conclude that if the entropy of the atmosphere decreases over height, or increases over depth, the blob becomes convectively unstable. Therefore, according to Equation (2.60), the condition of a blob to become convectively unstable in the polytropic atmosphere is

$$n < \frac{1}{\gamma - 1}. \tag{2.63}$$

If we choose γ as $5/3$, the medium becomes unstable if $n < 3/2$ and it is marginally stable if $n = 3/2$.

2.5.3 Mean-field modeling of turbulence

A flow can be turbulent if its Reynolds number is high enough. The Reynolds number in the convection zone of the Sun changes from about 10^{13} to 10^{12} from the bottom to the near surface of the Sun. Therefore it is believed that the convective motions in the convection zone are highly turbulent. Understanding the dynamics of the turbulent flow is still one of the important problems which has not been solved yet in fluid dynamics. An inevitable feature of the turbulent flow is the existence of the vortices of different sizes with different velocities, known as eddies. Studies have shown that large eddies are not stable structures in a turbulent fluid and they break down to the smaller ones. In this way, the energy is transported from large scales to a small scales. This breaking of eddies continues until the local Reynolds number becomes equal to unity, and the transported energy is transformed via viscosity into heat. Therefore, turbulence can affect the energy transport in the system. The complexity of studying turbulent motions is that the dynamics of the large scales are strongly tied to the dynamics of the small scales and there is no linear relation between them. Therefore, we need to model the dynamics of the turbulent motion. The model that we use in this thesis is known as the mean-field model. There, we divide the physical quantities of the fluid equations into two parts, namely a *mean* and a *fluctuating* part. For example, the velocity field can be written as $\boldsymbol{u} = \overline{\boldsymbol{U}} + \boldsymbol{u}'$. Then, we average all the fluid equations. A meaningful average procedure has to obey the *Reynolds rules* which are the following

$$\overline{\overline{\boldsymbol{U}}} = \overline{\boldsymbol{U}}, \qquad \overline{\boldsymbol{u}'} = 0, \qquad \overline{\overline{\boldsymbol{U}}\,\overline{\boldsymbol{U}}} = \overline{\boldsymbol{U}}\,\overline{\boldsymbol{U}}, \qquad \overline{\boldsymbol{u}_1' + \boldsymbol{u}_2'} = \overline{\boldsymbol{U}}_1 + \overline{\boldsymbol{U}}_2, \tag{2.64}$$

$$\overline{\frac{\partial \boldsymbol{u}}{\partial t}} = \frac{\partial \overline{\boldsymbol{U}}}{\partial t}, \qquad \overline{\frac{\partial \boldsymbol{u}}{\partial x_i}} = \frac{\partial \overline{\boldsymbol{U}}}{\partial x_i}, \qquad \overline{\overline{\boldsymbol{U}}\boldsymbol{u}'} = 0. \tag{2.65}$$

The process of this *Reynolds averaging* of the dynamical equations gives rise to higher order correlations which need to be modeled. At this point, we derive the mean-field equation of

the vector potential of the induction equation as an example to show how the mean field model works. We use (2.18) and decompose all quantities as follows

$$\frac{\partial(\overline{\boldsymbol{A}}+\boldsymbol{a}')}{\partial t}=(\overline{\boldsymbol{U}}+\boldsymbol{u}')\times(\overline{\boldsymbol{B}}+\boldsymbol{b}')-\mu_0\eta(\overline{\boldsymbol{J}}+\boldsymbol{j}'). \tag{2.66}$$

After averaging and applying the *Reynolds rules* we get

$$\frac{\partial\overline{\boldsymbol{A}}}{\partial t}=\overline{\boldsymbol{U}}\times\overline{\boldsymbol{B}}+\overline{\boldsymbol{\mathcal{E}}}-\mu_0\eta\overline{\boldsymbol{J}}, \tag{2.67}$$

where $\overline{\boldsymbol{\mathcal{E}}}=\overline{\boldsymbol{u}'\times\boldsymbol{b}'}$ is called the mean electromotive force and is a second order correlation term which can be modeled. One often-used model is given by

$$\overline{\boldsymbol{\mathcal{E}}}=\alpha\overline{\boldsymbol{B}}-\mu_0\eta_t\overline{\boldsymbol{J}}, \tag{2.68}$$

where both α and η_t are turbulent transport coefficients. In a very simple case of homogeneous and isotropic turbulence we have

$$\alpha=-\frac{1}{3}\overline{\boldsymbol{\omega}'\cdot\boldsymbol{u}'}\tau_{\rm c},\qquad \eta_t=\frac{1}{3}\overline{\boldsymbol{u}'^2}\tau_{\rm c}, \tag{2.69}$$

where $\boldsymbol{\omega}'=\boldsymbol{\nabla}\times\boldsymbol{u}'$ is the small-scale vorticity and $\tau_{\rm c}$ is a suitably defined correlation time (see e.g. Brandenburg & Subramanian, 2005). In our case, we do not consider a dynamo instability, hence $\alpha=0$ and we only have $\overline{\boldsymbol{\mathcal{E}}}=-\eta_t\overline{\boldsymbol{J}}$. The mean induction equation is then given by

$$\frac{\partial\overline{\boldsymbol{A}}}{\partial t}=\overline{\boldsymbol{U}}\times\overline{\boldsymbol{B}}-(\eta+\eta_t)\overline{\boldsymbol{J}}. \tag{2.70}$$

We follow the same procedure for all other equations that we want to solve in our problem. For the continuity and momentum equations we get

$$\frac{{\rm D}\overline{\rho}}{{\rm D}t} = -\overline{\rho}\boldsymbol{\nabla}\cdot\overline{\boldsymbol{U}}, \tag{2.71}$$

$$\overline{\rho}\frac{{\rm D}\overline{\boldsymbol{U}}}{{\rm D}t} = -\boldsymbol{\nabla}\overline{p}+\overline{\rho}\boldsymbol{g}+\overline{\boldsymbol{J}}\times\overline{\boldsymbol{B}}-(\tilde{\nu}+\nu_{\rm t})\overline{\boldsymbol{\mathcal{Q}}}, \tag{2.72}$$

where $\nu_{\rm t}$ is turbulent kinematic viscosity and we assume that both ν and $\nu_{\rm t}$ are constant in time and space, so

$$-\overline{\boldsymbol{\mathcal{Q}}}=\overline{\rho}(\nabla^2\overline{\boldsymbol{U}}+\frac{1}{3}\boldsymbol{\nabla}\boldsymbol{\nabla}\cdot\overline{\boldsymbol{U}}+2\overline{\boldsymbol{\mathsf{S}}}\boldsymbol{\nabla}\ln\overline{\rho}), \tag{2.73}$$

where we neglect additional terms involving correlation with fluctuating density. Here, $\overline{\boldsymbol{\mathcal{Q}}}$ is the mean stress divergence of the mean velocity field, analogues to Equation (2.6). Mean stresses due to small–scale velocity correlations are modeled using $\nu_{\rm t}\overline{\boldsymbol{\mathcal{Q}}}$. Another important property of the convection zone is that the fluid becomes opaque to the radiation and the energy is getting transported by the convective motions. This means that hot parcels from the hotter regions move adiabatically to the point that they mix with their surroundings

and dispose of their energy there. The convective flux quantifies the amount of enthalpy that is carried by the buoyant mass flux and is defined as

$$\overline{\boldsymbol{F}}_{\rm conv} = \overline{(\rho \boldsymbol{u})' c_{\rm p} T'}, \tag{2.74}$$

where $(\rho \boldsymbol{u})'$ and T' are fluctuating mass flux and temperature, respectively. We model $\overline{\boldsymbol{F}}_{\rm conv}$ as a function of $\boldsymbol{\nabla} s$,

$$\overline{\boldsymbol{F}}_{\rm conv} = -\chi_t \overline{\rho}\,\overline{T} \boldsymbol{\nabla} s, \tag{2.75}$$

where χ_t is the turbulent heat diffusivity. As an energy equation, we solve the equation of mean specific entropy, which is commonly thought to be of the form

$$\overline{\rho}\,\overline{T} \frac{{\rm D}\overline{s}}{{\rm D}t} = 4\pi\kappa\overline{\rho}(J - S) + \boldsymbol{\nabla} \cdot (\chi_{\rm t} \overline{\rho}\,\overline{T} \boldsymbol{\nabla} \overline{s}), \tag{2.76}$$

However, there is actually no reason for an temperature factor in the diffusion of entropy, so another form of the relevant evolution equation is

$$\overline{\rho} \frac{{\rm D}\overline{s}}{{\rm D}t} = \frac{4\pi\kappa\overline{\rho}}{\overline{T}}(J - S) + \boldsymbol{\nabla} \cdot (\chi_{\rm t} \overline{\rho} \boldsymbol{\nabla} \overline{s}) \qquad \text{(alternate form)}, \tag{2.77}$$

where J is the mean intensity (see Section 2.6.4) and S is the source function (see Section 2.6.1). The first term on the RHS is $-\boldsymbol{\nabla} \cdot \overline{\boldsymbol{F}}_{\rm rad}$ and the second one is $-\boldsymbol{\nabla} \cdot \overline{\boldsymbol{F}}_{\rm conv}$. The source function reads

$$S = \frac{\sigma_{\rm SB}}{\pi} \overline{T}^4. \tag{2.78}$$

2.6 Radiative transfer

In fluid dynamics, radiation appears in the energy equation where it plays the role of heating or cooling (Nordlund, 1982; Steffen et al., 1989; Vögler et al., 2005; Heinemann et al., 2006). One prominent example of this phenomenon is the granulation pattern at the surface of the Sun. There the dominant energy transport mechanism changes from convection to radiation. Consequently, radiation plays an important role in understanding the physics of the solar surface. Radiative energy is carried by photons with different energies (frequencies) and in the atmosphere of the star the photons interact with the plasma of the medium. These interactions of the photons with the medium are described by two processes named emission and absorption (extinction). In summery, we are interested in the amount of energy that is carried by radiation through the medium in a specific direction. This energy is defined by the quantity named *specific intensity* I_ν. The specific intensity of the radiation at position $\boldsymbol{x}$ is the energy that is carried by radiation per unit area, per unit time, per unit frequency ν, in a direction $\hat{\boldsymbol{n}}$, through a solid angle ${\rm d}\Omega$

$$I_\nu(\boldsymbol{x}, t, \hat{\boldsymbol{n}}) = \frac{{\rm d}E_\nu}{{\rm d}A\,{\rm d}t\,{\rm d}\nu\,{\rm d}\Omega}. \tag{2.79}$$

We can calculate I_ν using the radiative transfer equation

$$\hat{\boldsymbol{n}} \cdot \boldsymbol{\nabla} I_\nu = -\kappa_\nu \rho (I_\nu - S_\nu), \tag{2.80}$$

where κ_ν is opacity per unit mass and S_ν is the source function.

2.6.1 The source function

The source function is defined as $S_\nu = j_\nu/\alpha_\nu$, where j_ν is the emission coefficient and α_ν is the absorption coefficient. When photons and matter are in local thermodynamic equilibrium (LTE), the source function is given by[4]

$$S_\nu = B_\nu(T), \tag{2.81}$$

where B_ν is the Planck function. From the *Stefan-Boltzmann law* we know

$$B(T) = \int_0^\infty B_\nu d\nu = \frac{\sigma_{\rm SB}}{\pi} T^4, \tag{2.82}$$

where $\sigma_{\rm SB} = ac/4$ is the Stefan–Boltzmann constant, with a being the radiative constant and c the speed of light (see Table 5.1). As a result, the source function can be written as

$$S = \frac{\sigma_{\rm SB}}{\pi} T^4. \tag{2.83}$$

2.6.2 Kramers opacity law

The opacity κ_ν is the mass extinction coefficient and it determines the fraction of energy that is taken away from a beam per unit area per unit mass. As we see in Equation (2.80), it is important to know what the opacity of the medium is. This is a cumbersome task as all the details of the interaction of the photons and atoms in the medium should be taken into account. However, in stellar atmospheres, the opacity can locally be estimated based on the thermodynamical state. We adopt here the *Kramers opacity law*, which is given by

$$\kappa = \kappa_0 \rho^a T^b, \tag{2.84}$$

where κ_0 is a constant which depends on the chemical composition of the medium. In an atmosphere with a relatively low temperature, where free-free transition is a dominant processes $a = 1$ and $b = -7/2$. In the "generalized" Kramers opacity, a and b are free parameters and they can be determined by considering the relevant radiative processes. In hot stars the opacity is independent of density and temperature as the atmosphere of the star is completely ionized and electron scattering is the dominant processes, so $a = b = 0$. More important is the atmosphere of the Sun where the dominant opacity is due to H^- ions, a useful fit for this case is $a = 0.5$, $b = 7.7$ (see Table 2.1). The units of κ_0 are such that the units of κ always remain unit area per unit mass. Hence, the units of κ_0 will be different for different values of a and b; see Table 2.1.

2.6.3 Optical depth and length

In this thesis we want to model a solar–like transition from the convection zone to the atmosphere. This means a smooth transition from the optically thick convection zone to

[4]The source function based on the Einstein coefficient is given by $S_\nu = 2h\nu^3/c^2 \Big((g_u n_l - g_l n_u)/g_l n_u \Big)^{-1}$, where l and u stand for lower and upper level, g is the statistical weight. In LTE the Boltzmann distribution holds, therefore $S_\nu = B_\nu(T)$.

Table 2.1: Different Kramers opacities, following Equation (2.84)

Process	a	b	κ_0	units
Bound-free transition	1	-3.5	4.5×10^{24}	$\mathrm{cm}^5\,\mathrm{g}^{-2}\,\mathrm{K}^{7/2}$
Electron scattering	0	0	0.33	$\mathrm{cm}^2\,\mathrm{g}^{-1}$
H^-	0.5	7.7	$1.1 \times 10^{-25}\mathrm{Z}^{0.5}$	$\mathrm{cm}^{7/2}\,\mathrm{g}^{-3/2}\,\mathrm{K}^{-7.7}$

the optically thin atmosphere at the top of the convection zone. At this point, we introduce two parameters to model this transition. The first parameter is the *optical depth* τ which is frequency and angle dependent quantity. In the plane parallel atmosphere, along the radial direction, it is defined via (Rutten, 2003)

$$d\tau_{\mu\nu} \equiv -\kappa_\nu \rho \frac{dz}{|\mu|}, \tag{2.85}$$

where $\mu = \cos\theta$ with θ being the angle between the vertical of the atmosphere and the line of sight to the observer. For outgoing photons the angle is $\mu > 0$ and for incoming photons the angle is $\mu < 0$. If we use the *gray approximation*, in which opacity is independent of frequency, and measure τ in along the line of sight, we get

$$\tau(z) = \int_{z_0}^{\infty} \kappa\rho dz, \tag{2.86}$$

where z_0 is the position in the atmosphere $z = z_0$ and $z = \infty$ is the position of the observer where $\tau = 0$. The second parameter is the mean free path l_{mfp}, which is the path that a photon can travel without undergoing any interaction with matter, so

$$l_{\mathrm{mfp}} = \frac{1}{\kappa\rho}. \tag{2.87}$$

When l_{mfp} is smaller (larger) than other relevant thermodynamical length scale in the medium, the medium is optically thick $\tau > 1$ (optically thin $\tau < 1$). We can use the definition of the optical depth and rewrite Equation (2.80) as

$$\mu \frac{\mathrm{d}I}{\mathrm{d}\tau} = I - S. \tag{2.88}$$

2.6.4 Radiative flux

The radiative flux or the first moment of the intensity is

$$\boldsymbol{F}^{\nu}_{\mathrm{rad}} = \oint_{4\pi} I_\nu \hat{\boldsymbol{n}}\, d\Omega. \tag{2.89}$$

In order to solve the entropy equation (2.77), we want to compute $\boldsymbol{\nabla} \cdot \boldsymbol{F}_{\mathrm{rad}}$. By using Equation (2.80), we have

$$\begin{aligned} \boldsymbol{\nabla} \cdot \boldsymbol{F}_{\mathrm{rad}} &= \oint_{4\pi} d\Omega \int \hat{\boldsymbol{n}} \cdot \boldsymbol{\nabla} I_\nu \, d\nu \qquad (2.90) \\ &= -\oint_{4\pi} d\Omega \int \kappa_\nu \rho (I_\nu - S_\nu) d\nu, \qquad (2.91) \end{aligned}$$

We use the *gray approximation*, i.e., the frequency dependence of the parameters is neglected in the transfer equation. Moreover, the *mean intensity* J or zeroth moment of the intensity is defined as

$$J = \frac{1}{4\pi} \oint_{4\pi} I d\Omega. \qquad (2.92)$$

Therefore, we can write Equation (2.91) as

$$\boldsymbol{\nabla} \cdot \boldsymbol{F}_{\mathrm{rad}} = -4\pi\kappa\rho(J - S). \qquad (2.93)$$

Diffusion approximation

For an optically thick medium ($\tau \gg 1$), the radiative flux can be calculated by using the so called *diffusion approximation*

$$\boldsymbol{F}_{\mathrm{rad}} = -K \boldsymbol{\nabla} T, \qquad (2.94)$$

where T is the temperature and K is the radiative heat conductivity,

$$K = \frac{16\sigma_{\mathrm{SB}} T^3}{3\kappa\rho}. \qquad (2.95)$$

Chapter 3

The Models

As explained in Chapter 1, ultimately we want to investigate a possible mechanism of sunspot formation due to a turbulent magneto-thermal instability in the convection zone by including a radiative atmosphere at the top of the convection zone. For this, we need to prepare a medium which resembles the transition from the convection zone to the radiative surface of the Sun. This means that we should model a medium which has a smooth transition from an optically thick to an optically thin layer and has a stratification similar to that of the Sun. Therefore, we run some preparatory one-dimensional simulations to find the relevant stratified medium. We will explain the models used in the preparatory one-dimensional simulations before discussing the two-dimensional ones in Sections 3.3 and 3.4.

3.1 The Pencil Code

In this thesis, we use the Pencil Code to perform 1D simulations of radiative atmospheres as well as 2D simulations of radiative mean-field models. It is an open source code, multi–purpose and multi–user–developed, initiated by Brandenburg & Dobler (2002). It is maintained by google-code, `http://pencil-code.nordita.org`. In its typical configuration, it is a compressible MHD code which solves differential equations with a high-order finite-difference scheme. It is a parallel code written in *Fortran 90*. Moreover, it is a modular code. This modularity makes the Pencil Code being used in a vast range of astrophysical subjects such as planet formation (Johansen et al., 2007), solar dynamo models (Käpylä et al., 2012), coronal mass ejections (Warnecke et al., 2011), and combustion (Babkovskaia et al., 2011).

3.2 Radiative transfer in the Pencil Code

Solving the radiative transfer equation is not an easy task. Photons travel in all directions in the medium simultaneously, which is problematic to represent on a finite grid. Photons also propagate with the speed of light, which means it is a non-local problem. The Pencil Code overcomes the first problem by restricting the number of ray directions. The maximum number of rays that can currently be used in 3D for the problem at hand is 22 rays. The second problem has been solved by assuming that the source function is independent of the mean intensity. In other words, scattering has been ignored. This avoids solving the integro-differential form of the radiative transfer equation and enables us to discretize

the equation in a straightforward manner. The method that has been used in the PENCIL CODE can be categorized as a long characteristics method in solving the radiative transfer equation. In this method, by introducing predefined rays we can solve the radiative transfer problem along all rays to obtain the heating at each grid point (Kunasz & Auer, 1988). Hence it is possible to solve the transfer equation in a decomposed domain using the formal solution

$$I(\tau) = -\int_0^\tau e^{\tau'-\tau} S(\tau') d\tau'. \tag{3.1}$$

By splitting the calculation into two local parts that are computing-intensive, and one that is non-local but does not require any computation, so it is fast. We thus split the integral (3.1) into two parts,

$$I(\tau) = -\int_0^{\tau_0} e^{\tau'-\tau} S(\tau') d\tau' - \int_{\tau_0}^\tau e^{\tau'-\tau} S(\tau') d\tau', \tag{3.2}$$

which we refer to as an extrinsic part $I_{\rm extr}(\tau)$ that is computed on the neighboring processor and added in the last step, and an intrinsic part $I_{\rm intr}(\tau)$ that can be calculated immediately. However, the value of τ_0 in $I_{\rm intr}(\tau)$ is still unknown, so we only compute

$$I_{\rm intr}(\tilde{\tau}) = -\int_0^\tau e^{\tau'-\tilde{\tau}} S(\tau') d\tau' \tag{3.3}$$

and correct $\tau \to \tau_0 + \tilde{\tau}$ later in the last step. In the second step, we *communicate* the values of $\tau_0 = \tau$ and $I_0 = I_{\rm intr}(\tau_0)$ taken from the end of each ray on the previous processor, which cannot be done in parallel, but it does not take much time. In the final step we compute

$$I_{\rm extr}(\tau) = I_0 e^{\tau_0 - \tau} \tag{3.4}$$

and reassemble the final intensity as $I(\tau) = I_{\rm intr}(\tau) + I_{\rm extr}(\tau)$. Instead of solving the radiative transfer equation directly for the intensity, the contribution to the cooling rate $Q(\tau) = I(\tau) - S(\tau)$ is calculated instead, as was done also by Nordlund (1982). This avoids round-off errors in the optically thick part.

3.3 Modeling one-dimensional radiative atmosphere

3.3.1 Transition from optically thick to optically thin layers

In an optically thick medium where $\tau \gg 1$, the radiative flux $\boldsymbol{F}_{\rm rad}$ is given by

$$\boldsymbol{F}_{\rm rad} = -K \boldsymbol{\nabla} T. \tag{3.5}$$

In contrast, in an optically thin medium where $\tau \ll 1$, the radiative transfer Equation (2.80) should be solved explicitly. In a 1D simulation, we solve the transfer equation for two rays,

1. outgoing intensity, $\mu > 0$

$$+\frac{{\rm d}I^+}{{\rm d}\tau} = I^+ - S, \tag{3.6}$$

2. incoming intensity, $\mu < 0$

$$-\frac{\mathrm{d}I^-}{\mathrm{d}\tau} = I^- - S. \tag{3.7}$$

In the Pencil Code the radiative transfer equation is solved using the gray approximation and LTE assumption where the source function is equal to the Planck function, see Equation (2.83). We can use a similar method as Feautrier (1964), and introduce a mean intensity J and normalized flux H via

$$J = \frac{1}{2}(I^+ + I^-), \tag{3.8}$$

$$H = \frac{1}{2}(I^+ - I^-). \tag{3.9}$$

where the mean flux intensity J is the averaged over incoming and outgoing radiation. The flux H is the energy flux due to the differences of incoming and outgoing intensity. By adding and subtracting Equations (3.6) and (3.7), and using Equations (3.8) and (3.9), we get

$$\frac{\mathrm{d}J}{\mathrm{d}\tau} = H, \tag{3.10}$$

$$\frac{\mathrm{d}H}{\mathrm{d}\tau} = J - S, \tag{3.11}$$

where $d\tau$ is given by Equation (2.85). In the Pencil Code the radiative flux is given by $\boldsymbol{F}_{\rm rad} = (4\pi/3)H$. In the thermostatic equilibrium, the radiative flux is constant; see Equation (2.38). As a consequence H is also constant and $J = S$, accordingly. Therefore, by using Equation (2.83), (2.85) and (3.10), we can write $\boldsymbol{F}_{\rm rad}$ as

$$\boldsymbol{F}_{\rm rad} = -\frac{4\pi}{3}\frac{\sigma_{\rm SB}}{\pi}4T^3\frac{\mathrm{d}T}{\mathrm{d}\tau} = -\frac{16\sigma_{\rm SB}T^3}{3\kappa\rho}\frac{\mathrm{d}T}{\mathrm{d}z} \equiv -K\frac{\mathrm{d}T}{\mathrm{d}z}. \tag{3.12}$$

This equation shows that Equation (3.5) also describes the optically thin medium, but with a non-constant value of K, and only in the thermostatic case. We use the generalized Kramers opacity (see Section 2.6.2) to investigate the stratification of different radiative atmospheres.

3.3.2 Stratification with the generalized Kramers opacity

We model our 1D radiative atmosphere by expressing the radiative heat conductivity K by the generalized Kramers opacity as

$$K(\rho, T) = \frac{16\sigma_{\rm SB}T^{3-b}}{3\kappa_0\rho^{a+1}}. \tag{3.13}$$

As explained in Section 2.4, ρ is proportional to T^n in a polytropic atmosphere with polytropic index n. Interestingly, Equation (3.12) with $\boldsymbol{F}_{\rm rad} = \text{const}$, can be solved by $K(\rho, T) = \text{constant}$ and $\boldsymbol{\nabla}T = \text{const}$. A priori, this would not be compulsory, but it turns out that in many cases $K(\rho, T)$ is indeed constant in parts of the domain. In that case, the

Table 3.1: The different polytropic index n which is obtained by choosing different value of a and b in the generalized Kramers opacity.

a	b	n
1	-3.5	3.25
1	0	1.5
1	1	1
1	5	-1
-1	3	0/0

relation $K(\rho, T) = \text{const}$ implies a polytropic relationship when the polytropic index can be expressed as

$$n = \frac{3-b}{1+a}. \tag{3.14}$$

This relation can also be found in the work of Edwards (1990), but the author did not seem to consider the transition to an isothermal stratification. In addition, we can have a quasi–polytropic solutions if $K(\rho, T)$ is nearly constant.

Expressing the radiative heat conductivity based on the polytropic index gives us the opportunity to investigate the properties of both convectively stable and unstable radiative atmospheres (see Section 2.5) which we can extend into multi–dimensional simulations in future. We set the adiabatic index $\gamma = 5/3$, hence we have a convectively stable atmosphere if we choose a and b such as $n > 1.5$ and convectively unstable if $n < 1.5$; see Equation (2.63). We choose standard values of n in the astrophysical context which are listed in Table 3.1. Using smaller value than $n = -1$ would resemble an atmosphere where the pressure (and density) will increase over height, which is unphysical. For $-1 < n < 0$, only the density increases with height (temperature and pressure decrease with height), which means that the layer is top–heavy. This is a more extreme case of an unstable atmosphere. For the case $0 \leq n \leq 3/2$, the atmosphere is also unstable but not top heavy. We choose five different values of n, but in one case n is undefined. These parameters are as follows (see also Table 3.1 where the value of a and b are listed).

- $n = 3.25$, the Kramers opacity for the free–free and bound–free transition.
- $n = 1.5$, adiabatic stratification which is marginally Schwarzschild stable.
- $n = 1$, polytropic unstable.
- $n = -1$, ultra-unstable case.
- $n = 0/0$, the case of constant radiative heat conductivity where n is undefined.

Table 3.2: The units of the parameters are used in the 1D simulations.

quantities	code units	cgs units
height $[z]$	Mm	10^8 cm
velocity $[v]$	km s^{-1}	10^5 cm^{-1}
density $[\rho]$	g cm^{-3}	10^{-6} g cm^{-3}
temperature $[T]$	K	K
time $[t]$	ks	s

In the Pencil Code, κ is given by

$$\kappa = \tilde{\kappa_0}\left(\frac{\rho}{\rho_0}\right)^a\left(\frac{T}{T_0}\right)^b, \tag{3.15}$$

where ρ_0 and T_0 are reference density and temperature respectively, and they are constants. $\tilde{\kappa_0}$ is the rescaled opacity which is given by

$$\tilde{\kappa}_0 = \kappa_0 \rho_0^a \, \mathrm{T}_0^b, \tag{3.16}$$

with this choice, the units of $\tilde{\kappa_0}$ are independent of the exponents a and b. For each value of n, we choose 4 different values of $\tilde{\kappa_0} = 10^4, 10^5, 10^6, 10^7$ $\mathrm{Mm}^{-1}\,\mathrm{cm}^3\,\mathrm{g}^{-1}$. In the following, we use as length unit Mm and as velocity unit $\mathrm{km\,s}^{-1}$, and cgs units for density, temperature, and magnetic field. This implies that for us the units of $\tilde{\kappa_0}$ are $\mathrm{Mm}^{-1}\,\mathrm{cm}^3\,\mathrm{g}^{-1}$. The size of the domain for different values of n is different. We choose the size of the domain in such a way that we have a thin radiative atmosphere. If the domain is too big, it is difficult to obtain a solution by starting with an isothermal initial state; see below.

3.3.3 One-dimensional simulation setup

We run all 1D simulations using 512 grid points. The units of the parameters in our simulations are summarized in Table 3.2. We assume that the medium is completely ionized and we set the mean molecular weigh to $\mu = 0.6$. We calculate $c_\mathrm{p} \approx 0.035$ in code units by using Equation (2.27) which can be written as

$$c_\mathrm{p} = \frac{\mathcal{R}}{\mu}\frac{\gamma}{\gamma - 1} \tag{3.17}$$

We use a solar–like surface gravity $g = 274$ $(\mathrm{km/s})^2/\mathrm{Mm}$. All runs are initialized with an isothermal solution, which provides the density stratification is given by

$$\rho = \rho_0 \exp\big(-\frac{z}{H_\mathrm{p}}\big), \tag{3.18}$$

where ρ_0 is constant and we set it to $\rho_0 = 4 \times 10^{-4}$ g cm^{-3}. This value was chosen based on the value from a solar model at a depth of approximately 8 Mm below the surface. Furthermore, H_p is the scale height given by

$$H_\mathrm{p} = \frac{\mathcal{R}T}{\mu g} = \frac{c_\mathrm{s}^2}{\gamma g}. \tag{3.19}$$

In an isothermal atmosphere the temperature is constant and the sound speed $c_{\mathrm{s}0}$ is given by

$$c_\mathrm{s} = c_{\mathrm{s}0} = \left(\frac{\gamma R T_0}{\mu}\right)^{1/2}. \tag{3.20}$$

We take $c_\mathrm{s} = c_{\mathrm{s}0} = 30\,\mathrm{km\,s^{-1}}$ for the bottom boundary condition, which corresponds to the temperature $T_0 = 38,968\,\mathrm{K}$. Again, these values are based on those of a solar model. We set the incoming intensity, $I^- = 0$, at the top boundary and for the outgoing intensity $I^+ = S$ on the lower one. The gravitational potential is given by $\Phi = g(z - z_\infty)$ (see Section 2.4.2). Using Equation (3.19) and the definition of Φ we can rewrite Equation (3.18) as

$$\rho = \rho_0 \exp\left(-\gamma \frac{\Phi}{c_{\mathrm{s}0}^2}\right). \tag{3.21}$$

Therefore the density is $\rho = \rho_0$ at $z = z_\infty$. We use these values of T_0 and ρ_0 to calculate $\tilde{\kappa}_0$. For the bound-free transition see Table 2.1, we find corresponding value of our rescaled opacity $\tilde{\kappa_0} = 1.4 \times 10^{13}$ Mm^{-1} cm^3 g^{-1}. We solve the following equations:

$$\frac{\mathrm{D}\ln\rho}{\mathrm{D}t} = -\boldsymbol{\nabla}\cdot\boldsymbol{u}, \qquad \text{(continuity equation)} \tag{3.22}$$

$$\rho\frac{\mathrm{D}\boldsymbol{u}}{\mathrm{D}t} = -\boldsymbol{\nabla}p + \rho\boldsymbol{g}, \qquad \text{(momentum equation)} \tag{3.23}$$

$$\rho T\frac{\mathrm{D}s}{\mathrm{D}t} = 4\pi\kappa\rho(J - S) + 2\nu\rho\mathbf{S}^2, \qquad \text{(entropy equation)} \tag{3.24}$$

We use equation state of an ideal gas as $p = (c_\mathrm{v} - c_\mathrm{p})\rho T$. In all our calculations, we ignore the second part of Equation (3.24), as we choose the value of viscosity to be small.

3.4 Modeling two-dimensional magneto-thermal instability

We perform a two-dimensional simulation in a Cartesian domain of size $10 \times 5\,\mathrm{Mm}^2$. We solve the equations of the mean-field magnetohydrodynamics (see Section 2.5.3) including radiative transfer equation which is explained in Sections 2.6 and 2.6.4

$$\frac{\partial\overline{\boldsymbol{A}}}{\partial t} = \overline{\boldsymbol{U}}\times\overline{\boldsymbol{B}} - (\eta_t + \eta)\overline{\boldsymbol{J}}, \qquad \text{(induction equation)} \tag{3.25}$$

$$\overline{\rho}\frac{\mathrm{D}\overline{\boldsymbol{U}}}{\mathrm{D}t} = \overline{\boldsymbol{J}}\times\overline{\boldsymbol{B}} - (\nu_\mathrm{t} + \nu)\overline{\boldsymbol{\mathcal{Q}}} - \boldsymbol{\nabla}\overline{p} + \overline{\rho}\boldsymbol{g}, \qquad \text{(momentum equation)} \tag{3.26}$$

$$\overline{\rho}\frac{\mathrm{D}\overline{s}}{\mathrm{D}t} = \frac{4\pi\kappa\overline{\rho}}{\overline{T}}(J - S) + \boldsymbol{\nabla}\cdot(\chi_\mathrm{t}\overline{\rho}\boldsymbol{\nabla}\overline{s}), \qquad \text{(entropy equation)} \tag{3.27}$$

$$\frac{\mathrm{D}\overline{\rho}}{\mathrm{D}t} = -\overline{\rho}\boldsymbol{\nabla}\cdot\overline{\boldsymbol{U}}, \qquad \text{(continuity equation)} \tag{3.28}$$

where $\mathrm{D}/\mathrm{D}t = \partial/\partial t + \overline{\boldsymbol{U}} \cdot \boldsymbol{\nabla}$ is the advective derivative, $\overline{\boldsymbol{B}} = \boldsymbol{\nabla} \times \overline{\boldsymbol{A}} + \hat{\boldsymbol{y}} B_0$ is the mean magnetic field with an imposed constant field pointing in the y direction, The intensity is obtained by solving

$$\hat{\boldsymbol{n}} \cdot \boldsymbol{\nabla} I = -\kappa \overline{\rho} (I - S). \tag{3.29}$$

We solve the radiative transfer equation along a set of 8 rays, namely $\hat{\boldsymbol{n}} = (\pm 1, 0, 0)$, $\hat{\boldsymbol{n}} = (0, 0, \pm 1)$, and $\hat{\boldsymbol{n}} = (\pm 1, 0, \pm 1)/\sqrt{2}$. We assume LTE, and use the Kramers opacity by choosing $a = b = 1$ which corresponds to the polytropic index $n = 1$. We use a perfect gas with the following equation of state

$$\overline{p} = (c_p - c_v) \overline{\rho} \overline{T} = e^{\overline{s}/c_v} \overline{\rho}^{\gamma}, \tag{3.30}$$

3.4.1 Turbulent heat transport

Following Kitchatinov & Mazur (2000), we assume that χ_{t} is quenched by the magnetic field. We adopt a simplified quenching law of the form

$$\chi_{\mathrm{t}} = \chi_{\mathrm{t}0} / (1 + Q_\chi \overline{\boldsymbol{B}}^2 / B_{\mathrm{eq}}^2), \tag{3.31}$$

where $B_{\mathrm{eq}}^2 = \mu_0 \overline{\rho} u_{\mathrm{rms}}^2$ is the *equipartition magnetic field* and it depends on height through $\overline{\rho}$, but we assume that the u_{rms} stays constant. Here, Q_χ is a constant quenching parameter and $\chi_{\mathrm{t}0}$ is a constant without influence of the magnetic field B. We implement χ_{t} in the *mean field module* in the Pencil Code. If we consider (3.27) and focus on the second part we have

$$\frac{\mathrm{D}\overline{s}}{\mathrm{D}t} = \chi_{\mathrm{t}0} (\boldsymbol{\nabla} \ln \overline{\rho} + \boldsymbol{\nabla} \ln \chi_{\mathrm{t}}) \cdot \boldsymbol{\nabla} \overline{s} + \nabla^2 \overline{s}. \tag{3.32}$$

For the sake of simplicity, we introduce $\beta = |\overline{\boldsymbol{B}}| / B_{\mathrm{eq}}$. $\boldsymbol{\nabla} \ln \chi_{\mathrm{t}}$ is calculated as

$$\begin{aligned}
\boldsymbol{\nabla} \ln \chi_{\mathrm{t}} &= -(1 + Q_\chi \beta^2)^{-1} \boldsymbol{\nabla} (Q_\chi \beta^2), && (3.33)\\
&= -(1 + Q_\chi \beta^2)^{-1} Q_\chi (2 \overline{B}_k \overline{B}_{k,i} / B_{\mathrm{eq}}^2 - (\beta^2) \boldsymbol{\nabla} \ln \rho), && (3.34)\\
&= -(1 + Q_\chi \beta^2)^{-1} \frac{Q_\chi}{B_{\mathrm{eq}}^2} (2 \overline{B}_k \overline{B}_{k,i} - \overline{B}^2 \boldsymbol{\nabla} \ln \rho) && (3.35)
\end{aligned}$$

3.4.2 Boundary conditions

We choose perfect conductor boundary conditions at top and bottom of the domain for the magnetic field as

$$\overline{B}_z = 0, \overline{J}_x = \overline{J}_y = 0, \tag{3.36}$$

by setting

$$\overline{A}_x = \overline{A}_y = \overline{A}_{z,z} = 0, \tag{3.37}$$

and stress-free boundary condition for the velocity field as

$$\overline{U}_{x,z} = \overline{U}_z = 0. \tag{3.38}$$

Table 3.3: The units of the parameters are used in the 2D simulations.

quantities	code units	cgs units
height $[z]$	Mm	10^8 cm
velocity $[\overline{U}]$	km s^{-1}	10^5 cm^{-1}
density $[\overline{\rho}]$	$10^{-6}\,\mathrm{g\,cm^{-3}}$	10^{-6} g cm^{-3}
temperature $[\overline{T}]$	K	K
time $[t]$	ks	s
Magnetic field $[\overline{B}]$	G	G
gravitational acceleration $[g]$	km^2 s^{-2} Mm^{-1}	10^2 cm^2 s^{-2}

We choose periodic boundary conditions in the horizontal direction. At the bottom we fix temperature and its vertical derivative, as the same as in our 1D simulations. We choose the same boundary condition for the intensity and temperature as our 1D simulation,

$$I^+ = S, \qquad I^- = 0, \qquad \mathrm{d}T/\mathrm{d}z = \mathrm{const}, \qquad T(z_{\mathrm{bot}}) = \mathrm{const}. \tag{3.39}$$

We summarize the units of our simulation is Table 3.3.

The units of the constant parameter in our simulation is $\mu_0 = 4\pi\times10^{-2}\,\mathrm{kG^2\,km^{-2}\,s^2\,\mu g^{-1}\,cm^3}$. Furthermore, $\sigma_{\mathrm{SB}} = 5.67\times10^{-14}\,\mu\mathrm{g\,cm^{-3}\,km^3\,s^{-3}\,K^{-4}}$ and $c_p = 0.0208\,\mathrm{km^2\,s^{-2}\,K^{-1}}$. We use a gravitational acceleration whose value is motivated by the Sun, namely $g = 274\,\mathrm{km^2 s^{-2}\,Mm^{-1}}$. Our initial stratification is that of a polytropic with polytropic index $n = 3/2$, corresponding to marginally stable stratification, $\mathrm{d}\overline{T}/\mathrm{d}z = -g/c_p \approx 13,200\,\mathrm{K\,Mm^{-1}}$. Initially we considered a domain $0 \le z \le 4\,\mathrm{Mm}$ such that the polytrope would reach vanishing temperature at $z = 4.5\,\mathrm{Mm}$. This corresponds to a temperature at $z = 0$ of $59,300\,\mathrm{K}$. To transport convective flux, we chose an unstable polytrope with $n = 1$, keeping however the temperature and its gradient at $z = 0$ fixed and we extended the domain to $0 \le z \le 5\,\mathrm{Mm}$. We choose the polytropic index $n = 1$ by taking $a = b = 1$. Furthermore, we take $\tilde{\kappa_0} = 100\,\mu\mathrm{g^{-1}\,cm^3\,Mm^{-1}}$. The resulting value of $\tau = 1$ turned then out to be at $z \approx 3\,\mathrm{Mm}$. We monitor the value of the turbulent Rayleigh number,

$$\widetilde{\mathrm{Ra}} = \frac{gd^4}{\nu_{\mathrm{t}}\chi_{\mathrm{t0}}}\left(-\frac{\mathrm{d}\overline{s}/c_p}{\mathrm{d}z}\right)_{z=z_1} \tag{3.40}$$

at $z = z_1 \equiv 1\,\mathrm{Mm}$, where d is the value of z where $\tau = 1$, which corresponds to $d \approx 3\,\mathrm{Mm}$.

For the rms velocity of the turbulence we chose $u_{\mathrm{rms}} = 0.1\,\mathrm{km/s}$. This also defines the value of the equipartition field strength, $B_{\mathrm{eq}} = u_{\mathrm{rms}}\sqrt{\mu_0\overline{\rho}}$. With $\overline{\rho} = 1.7\,\mu\mathrm{g\,cm^{-3}}$ at $\tau = 1$ we have $B_{\mathrm{eq}} = 46\,\mathrm{G}$. We use a numerical resolution of 512×256 mesh points and a fixed time step of $5\times10^{-6}\,\mathrm{ks}$, corresponding to $0.005\,\mathrm{s}$.

Chapter 4

Results

4.1 Results of one-dimensional radiative atmosphere

We perform simulations with a resolution of 512 grid points using five sets of values for the exponents a and b in the expression for the Kramers opacity; see Equation (3.15). Each set of runs is denoted by a letter A–D. For all sets of runs, we keep $a = 1$ and change the value of b from $-7/2$, to 1, 0, and 5. For each of these sets, we perform four runs that differ only in the values of $\tilde{\kappa_0}$. The numeral on the label of each run refers to a different value of $\tilde{\kappa_0}$. In set A, we use $a = 1$ and $b = -7/2$. Runs A4, A5, A6 and A7 correspond to $\tilde{\kappa_0}$ equal to 10^4, 10^5, 10^6 and 10^7 $\mathrm{Mm}^{-1}\,\mathrm{cm}^3\,\mathrm{g}^{-1}$, respectively. All the other designations follow the same system. All runs have been started with the same initial isothermal condition. However, the size of the domain changes, as will be discussed in Section 4.1.9. In Figure 4.1, both the initial temperature and the initial density are plotted normalized by their values at the bottom. The temperature is constant in space and the density decreases exponentially with height. All runs show the same equilibrium state after a sufficient amount of running time, and the obtained profiles of temperature, density and entropy have a nearly polytropic stratification in the lower part of the domain and a nearly isothermal stratification in the upper part of the domain. An exception are the runs of set E where the polytropic index is undefined ($n = 0/0$). We summarize the important quantities obtained from all runs in Table 4.1. These quantities are calculated in the equilibrium state. All runs show a similar evolution of density, temperature and entropy. In the next sections we describe these quantities in more detail.

4.1.1 Temperature stratification

For all runs, the initial isothermal temperature stratification does not stay isothermal. During the simulation the temperature cools down, starting at the upper boundary, near the anticipated location of $\tau \approx 1$, where the cooling is most efficient. After a certain time the temperature reaches an equilibrium state. The temperature profile can be divided into two distinguishable parts, a nearly polytropic part which starts from the bottom of the domain and extends to a certain height, and a nearly isothermal part which starts from this height and extends to the top of the domain. The transition of the temperature from the initial state to the equilibrium state follows a specific pattern, which is the same for all the runs. We plot the evolution of the temperature profile of run A6 in Figure 4.2 as an explanatory case $\tilde{\kappa_0} = 10^6$ $\mathrm{Mm}^{-1}\,\mathrm{cm}^3\,\mathrm{g}^{-1}$. The temperature starts decreasing close to the top boundary, where the radiation is acting as an efficient cooling process. Already after

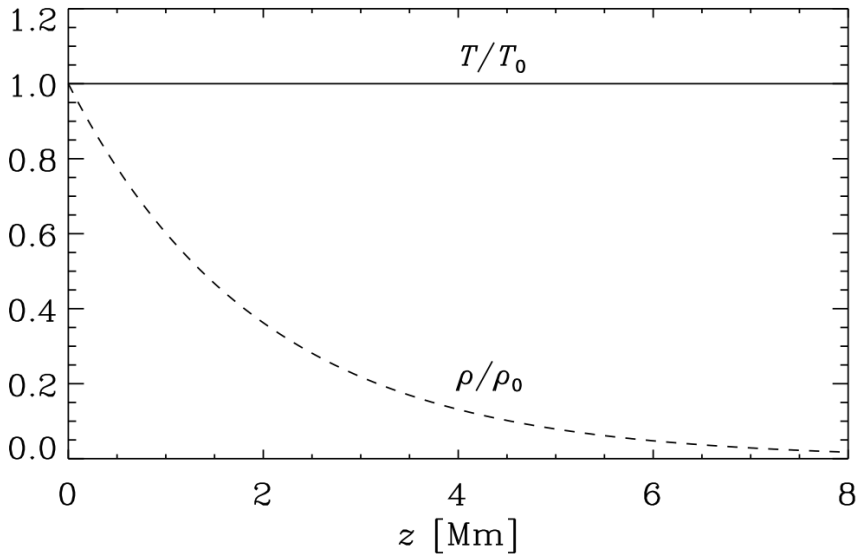

Figure 4.1: Initial conditions of temperature and density for all of the runs. The solid line shows the initial temperature profile that is normalized by T_0 and the dashed line presents the initial density profile normalized by ρ_0 plotting over height, where the subscript 0 indicates the values at the bottom of the domain.

a short time of $t = 1\,\mathrm{ks}$ (20 min), the temperature has decreased by more than half of the initial value of temperature at the top boundary and follows a polytropic solution in most of the domain where the temperature gradient has a similar value than in the equilibrium state. At $t = 10\,\mathrm{ks}$ (3 hours), close to the upper boundary, an isothermal part seems to appear. However, it takes more than $t = 500\,\mathrm{ks}$ (6 days) until the equilibrium solution is reached with a prominent isothermal part of $T \approx 7000$ K. The higher the value of $\tilde{\kappa_0}$, the lower the temperature is in the isothermal part and the longer it takes to reach this state. Increasing the normalized opacity $\tilde{\kappa_0}$ by three orders of magnitudes results in a factor of five for set A and a factor of three in case D. As the exponent b changes from the smallest value in set A to the largest one in set D, the slope of the temperature decreases with height. This means that the polytropic part of the atmosphere is smaller for larger values b. Note that the size of the domain is chosen larger for smaller b. For sets A, B and C in the polytropic part, the temperature is almost the same for different values of opacity $\tilde{\kappa_0}$. However, for the lowest value of $\tilde{\kappa_0}$ the temperature deviates somewhat. But in set D, for different values of opacity, the slope of the temperature is different for each value of $\tilde{\kappa_0}$. The isothermal temperatures also show a dependency on b. For $\tilde{\kappa_0} = 10^4\ \mathrm{Mm^{-1}\,cm^3\,g^{-1}}$ the temperature in run A4 is $T \approx 2.2 \times 10^4\,\mathrm{K}$, whereas in run D4 the value is $T \approx 2.9 \times 10^4\,\mathrm{K}$. A similar behavior can also be seen for the other values of $\tilde{\kappa_0}$. Next, we calculate the optical depth for all runs using Equation (2.86). We find that the transition point from the polytropic part to the isothermal part coincides with the $\tau \approx 1$ surface. We illustrate the surface $\tau \approx 1$ by red dots in all plots of temperature in Figure 4.3. The polytropic solution corresponds to the optically thick part with $\tau > 1$ and the isothermal part corresponds

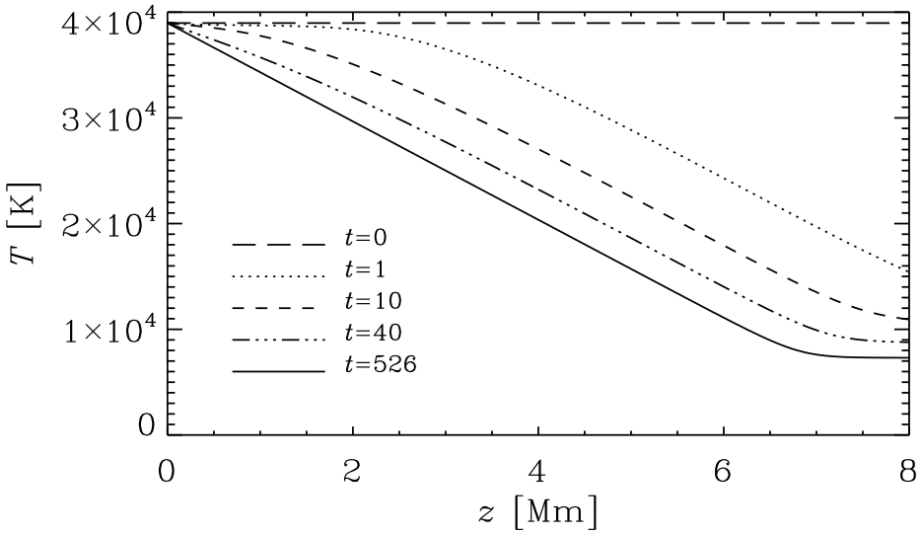

Figure 4.2: Temperature profile over height z for five different times $t = 0, 1, 10, 40$, and 526 ks for run A4 with $\tilde{\kappa_0} = 10^6$ Mm^{-1} cm^3 g^{-1}.

to the optically thin part with $\tau < 1$. For each set, the transition point depends on the value of $\tilde{\kappa_0}$. As we go from smaller to larger values of $\tilde{\kappa_0}$, the surface is shifted to larger heights and the surface becomes cooler. This is due to the fact that the radiative heat conductivity K has an inverse relation with $\tilde{\kappa_0}$ and is directly proportional to the flux. Therefore, by increasing the value of $\tilde{\kappa_0}$, K decreases and as a consequence radiative flux also decreases. By decreasing the flux, the effective temperature decreases as $T_{\rm eff} \propto F_{\rm rad}^{1/4}$. This means that the temperature at the surface is smaller for larger values of $\tilde{\kappa_0}$. This shows that the opacity is an important quantity. In other words, for each set of runs the value of $\tilde{\kappa_0}$ determines at which temperature and at which height the atmosphere becomes isothermal; see the middle column of Figure 4.3. The $\tau \approx 1$ surfaces lie for set A on the polytropic temperature profile. But by increasing b, the location of the surfaces differ from the polytropic temperature profile.

4.1.2 Density stratification

In the first column of Figure 4.3, we plot the density profile for all sets of runs. For all runs, the density profile decreases sharply in the upper part where $\tau < 1$. In all sets, as we go from the smallest value of $\tilde{\kappa_0}$ to the largest one, the stratification in the isothermal part becomes stronger. As we increase b from -3.5 to 0, 1, and 5 for sets A, B, C, and D, respectively, the density contrast becomes smaller. For example, as a comparison, we calculate the density contrast of runs B7 and C7 from the bottom to the surface, which are ≈ 23 and ≈ 8, respectively. All runs show small departures from their initial state in the optically thick part, but strong departures in the optically thin part. This is due to the fact that close to the surface, temperature decreases due to the radiative cooling. Therefore the density also decreases. As we go from lower opacities to higher ones, the

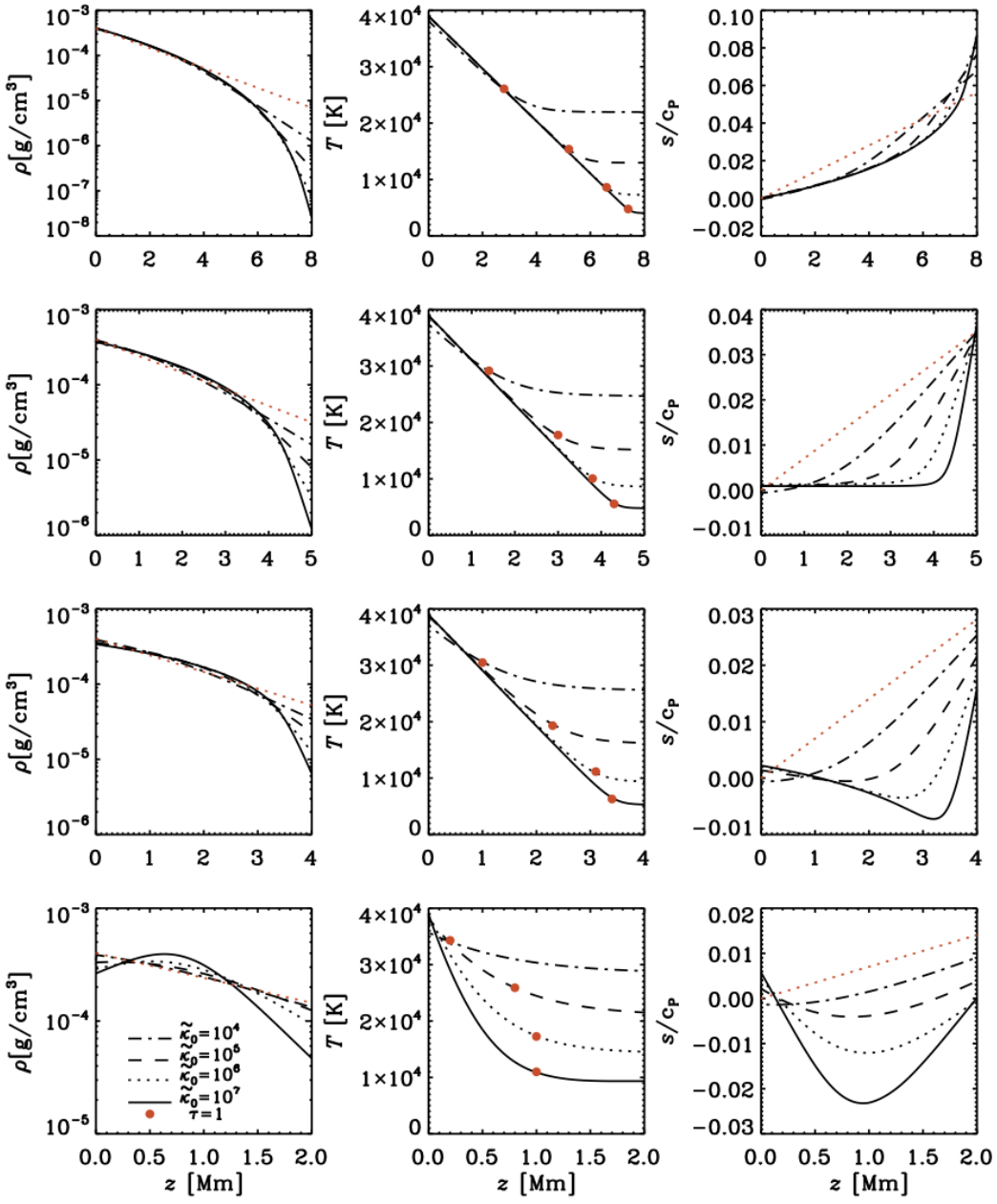

Figure 4.3: Density, temperature and entropy of the equilibrium state over height, from left to right, for four sets of runs A, B, C and D, from top to bottom. The four different lines in each plot corresponds to the value of the rescaled opacity $\tilde{\kappa_0} = 10^4$, 10^5, 10^6, 10^7 $\mathrm{Mm}^{-1}\,\mathrm{cm}^3\,\mathrm{g}^{-1}$. The red dots in the temperature plots represent the surface $\tau \approx 1$. The red dotted lines in the density and entropy plots represent the initial profile of each set, respectively.

steepness of the density increases. The density for set D shows a slightly different profile compared to the other sets of runs. In sets A, B, and C the density profiles are almost the same in the polytropic part. But in set D the profiles are not the same, in particular for run D7 the density has a maximum close to the middle of the domain. This maximum is just below the $\tau \approx 1$ surface. The reason for that is that the density in this case is related to temperature as $1/T$. At the bottom where the temperature is higher, the density decreases. This density reaches its maximum where the entropy has a minimum. This can be explained by the relation of temperature, density and entropy. By using Equations (2.29) and (3.20), the temperature can be written as

$$T = \frac{c_{\rm s0}^2}{c_{\rm p}(\gamma-1)} \exp\left(\frac{\gamma s}{c_{\rm p}} + (\gamma-1)\ln\frac{\rho}{\rho_0}\right). \tag{4.1}$$

As we see in the last row of Figure 4.3 for run D7, the temperature is still decreasing where the density has its maximum. The density starts decreasing more strongly where the temperature starts to remain constant. In order to keep the temperature constant in Equation (4.1), the entropy starts to increase where the density is decreasing. This can be explained according to the inverse relation of density with temperature.

In the multi-dimensional case convection is possible. Therefore, the atmosphere would become convectively unstable and would start to mix material and approach the adiabatic state where $\rho \propto T^{3/2}$.

4.1.3 Entropy stratification

We plot the entropy profiles for all sets of runs in the equilibrium state in the last column of Figure 4.3. The entropy decreases for about half of the runs in the polytropic part and starts to increase in the isothermal part. All runs show a positive vertical entropy gradient, $\nabla_z s > 0$, in the isothermal part, but not in the polytropic part. In this lower part, for set A, the entropy gradient is positive, $\nabla_z s > 0$, in set B it is constant and equal to zero, $\nabla_z s \approx 0$. This shows that for set B, the atmospheres are isentropic. In sets C and D, except for the case $\tilde{\kappa_0} = 10^4$ Mm^{-1} cm^3 g^{-1}, the entropy gradient is negative, $\nabla_z s < 0$. This means that their atmospheres are convectively unstable. In set D the entropy gradients are larger than in case C where their atmospheres are marginally unstable; see Section 2.5.1. But in the isothermal part of set C, the entropy gradient is much larger than in set D. For each set of runs, as we go from smaller values of $\tilde{\kappa_0}$ to larger ones, the entropy profiles have stronger gradients. All these results can be explained according to Equation (4.1). In the isothermal part, where the density decreases sharply, the entropy has to increase to keep the temperature constant in Equation (4.1). As explained in Section 4.1.2, the density drops more strongly for the higher the value of $\tilde{\kappa_0}$ is in each set. Therefore, entropy increases more strongly as well, compared to the cases with smaller values of $\tilde{\kappa_0}$. In Figure 4.4, we plot the gradient of entropy over height expressed in terms of the square of the Brunt-Väisälä frequency $N_{\rm BV}^2 = -\boldsymbol{g}.\boldsymbol{\nabla} s/c_{\rm p}$ and normalized by $c_{\rm s}^2/H_{\rm p}^2$. If the atmosphere is stably stratified, $\boldsymbol{g}\cdot\boldsymbol{\nabla} s/c_{\rm p}$ is negative and if it is convectively unstable, $\boldsymbol{g}\cdot\boldsymbol{\nabla} s/c_{\rm p}$ is positive. This can also be expressed as a modified Rayleigh number

$$\widetilde{\rm Ra} = {\rm Pr}\,{\rm Ra}\,({\rm Ma}/{\rm Pe})^2, \tag{4.2}$$

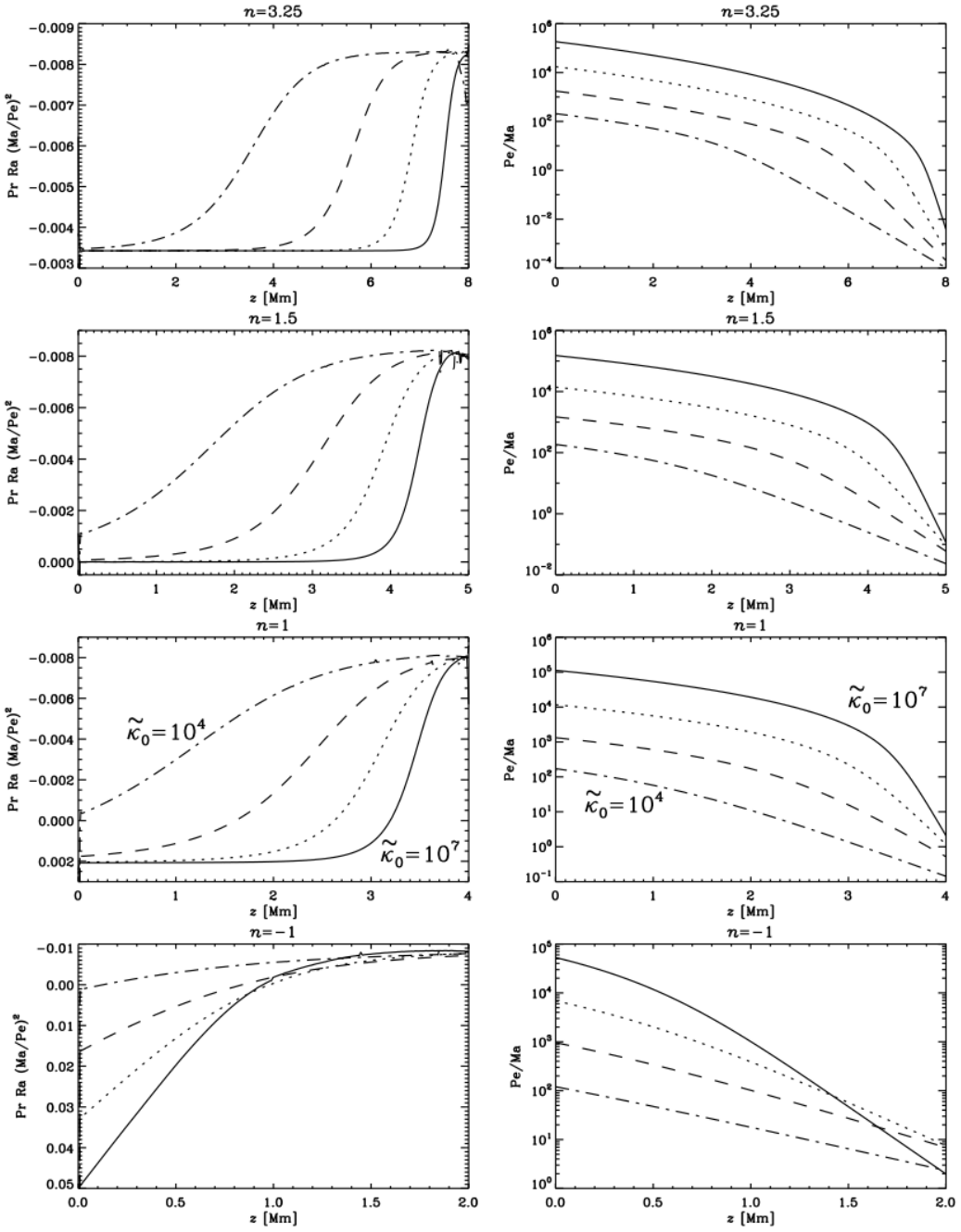

Figure 4.4: $\widetilde{\mathrm{Ra}}$ (left panels) and $\widetilde{\mathrm{Pe}}$ (right panels) over height for four sets of runs A, B, C, and D from the top to the bottom. In each plot $\widetilde{\mathrm{Ra}}$ is plotted for different values of $\tilde{\kappa_0}$ as $\tilde{\kappa_0} = 10^4$ $\mathrm{Mm}^{-1}\,\mathrm{cm}^3\,\mathrm{g}^{-1}$ (dotted-dashed line), $\tilde{\kappa_0} = 10^5$ $\mathrm{Mm}^{-1}\,\mathrm{cm}^3\,\mathrm{g}^{-1}$ (dashed line), $\tilde{\kappa_0} = 10^6$ $\mathrm{Mm}^{-1}\,\mathrm{cm}^3\,\mathrm{g}^{-1}$ (dotted line) and $\tilde{\kappa_0} = 10^7$ $\mathrm{Mm}^{-1}\,\mathrm{cm}^3\,\mathrm{g}^{-1}$ (solid line).

Table 4.1: Summary of the runs. In the table, the size of the domain $z_{\rm top}$ in units of Mm, the density at the surface $\rho_{\tau=1}$ in units of $\mathrm{g\,cm^{-3}}$, the height of the surface $z_{\tau=1}$ in Mm, the thermal adjustment time $\tau_{\rm adjust}$ in ks, the effective temperature $T_{\rm eff}$ in K and radiative heat conductivity at the bottom of the domain $K_{\rm bot}$ in $\mathrm{g\,cm^{-3}\,K^{-1}\,Mm^{-1}\,km^3\,s^{-3}}$ the normalized opacity are $\tilde{\kappa_0} = \kappa_0 \rho_0^a T_0^b$ is in units of $\mathrm{Mm^{-1}\,cm^3\,g^{-1}}$ shown for each run. The second to the sixth columns show quantities which are input parameters to the models whereas the quantities in last five columns are the results of the simulations, computed from the equilibrium state.

Run	a	b	n	$\tilde{\kappa_0}$	$z_{\rm top}$	$z_{\tau=1}$	$\rho_{\tau=1}$	$\tau_{\rm adjust}$	$T_{\rm eff}$	$K_{\rm bot}$
A4	1	-3.5	3.25	10^4	6	2.8	1.0×10^{-4}	15	23,602	3.9×10^{-6}
A5	1	-3.5	3.25	10^5	8	5.2	1.7×10^{-5}	29	13,900	4.6×10^{-7}
A6	1	-3.5	3.25	10^6	8	6.6	2.5×10^{-6}	226	7,800	4.6×10^{-8}
A7	1	-3.5	3.25	10^7	8	7.4	3.7×10^{-7}	4990	4,400	4.4×10^{-9}
B4	1	0	1.5	10^4	5	1.4	2.2×10^{-4}	13	26,566	4.53×10^{-6}
B5	1	0	1.5	10^5	5	2.9	9.0×10^{-5}	18	16,304	5.15×10^{-7}
B6	1	0	1.5	10^6	5	3.8	3.7×10^{-5}	120	9,306	5.38×10^{-8}
B7	1	0	1.5	10^7	5	4.3	1.6×10^{-5}	1674	5,162	5.08×10^{-9}
C4	1	1	1	10^4	4	1	2.6×10^{-4}	2.3	27,579	5.1×10^{-6}
C5	1	1	1	10^5	4	2.3	1.3×10^{-4}	7.4	17,467	5.6×10^{-7}
C6	1	1	1	10^6	4	3.1	7.0×10^{-5}	78	10,119	6.0×10^{-8}
C7	1	1	1	10^7	4	3.4	3.9×10^{-5}	712	5,730	6.1×10^{-9}
D4	1	5	-1	10^4	2	0.2	3.6×10^{-4}	2.1	31,003	1.1×10^{-5}
D5	1	5	-1	10^5	2	0.8	2.8×10^{-4}	2.2	23,118	1.3×10^{-6}
D6	1	5	-1	10^6	2	1	2.8×10^{-4}	27	15,647	1.9×10^{-7}
D7	1	5	-1	10^7	2	1	3.2×10^{-4}	241	10,099	3.1×10^{-8}
E4	-1	3	0/0	10^4	4	3.0	8.7×10^{-5}	1.9	23,681	4.47×10^{-6}
E5	-1	3	0/0	10^5	4	3.6	5.6×10^{-5}	15	14,897	4.47×10^{-7}
E6	-1	3	0/0	10^6	4	3.8	3.9×10^{-5}	141	8,821	4.47×10^{-8}
E7	-1	3	0/0	10^7	10	–	–	–	–	–

where $\mathrm{Pr} = \nu/\chi$ is the Prandtl number defined as the ratio of viscosity over thermal diffusivity. It turns out that the parameter number combination $\mathrm{Pr\,Ra\,(Ma/Pe)^2}$ changes very little. This means that $\mathrm{Pr\,Ra}$ is inversely proportional to $\mathrm{(Ma/Pe)^2}$. For example, for $n = 1$ we have $\mathrm{Pr\,Ra\,(Ma/Pe)^2} = 0.002$, and $\mathrm{Pe/Ma} \approx 10^5$ (see Figure 4.4), so $\mathrm{Pr\,Ra} \approx 2 \times 10^7$, which is quiet feasible with present day simulations.

4.1.4 Radiative cooling

As explained in Section 4.1.1, the temperature starts to cool down first in the upper part of the domain where $\tau \approx 1$ and it reaches its thermostatic equilibrium where there exists a nearly polytropic part for $\tau > 1$ and a nearly isothermal part for $\tau < 1$. Radiative cooling is strong near the surface, but is less efficient as we go far from the surface. The reason for the strong radiative cooling in the upper part of the domain where $\tau \approx 1$ is related to the initial isothermal stratification. For a constant temperature, the opacity increases with density; see Equation (3.15). A lower opacity leads to a stronger radiation. In the initial condition for all sets (see Figure 4.1), the density decreases over height; see Equation (3.21). The decrease of density leads to a decrease of opacity. Therefore, the mean free path of the photons (see Equation (2.87)) increases and the radiative cooling becomes more efficient. As the temperature starts to cool down, the density decreases further as it is related to the temperature in each set via

$$\rho \propto T^{(3-b)/2}. \tag{4.3}$$

This means that for sets A, B, and C, the decrease of density corresponds to a decrease of temperature. As we go from set A to set D, the value of b increases, so the density decreases less steeply. As a consequence, the value of the temperature in the equilibrium solution of the isothermal part for the same value of $\tilde{\kappa_0}$ decreases from set A to set D (compare A7 and B7, for example). The cooling process continues to the point that the atmosphere reaches thermostatic equilibrium, $\boldsymbol{\nabla} \cdot \boldsymbol{F}_{\rm rad} = 0$. This is expected because we inject a constant flux from the lower boundary of the domain. The equilibrium solution can be explained using the energy Equation (3.24) and also the moments of the intensity. The zeroth and the first moments are defined in Equations (2.92) and (2.89). The second moment of the intensity is given by

$$\mathsf{P}_{\rm rad} = \frac{1}{4\pi} \int_{4\pi} I \hat{\boldsymbol{n}} \hat{\boldsymbol{n}} \, \mathrm{d}\Omega, \tag{4.4}$$

where $\mathsf{P}_{\rm rad}$ is the radiation pressure tensor, and

$$\boldsymbol{\nabla} \cdot \mathsf{P}_{\rm rad} = -\kappa \rho \boldsymbol{F}_{\rm rad}. \tag{4.5}$$

We use the Eddington approximation which is an approximation to close these moment equations. It is given by

$$\boldsymbol{\nabla} \cdot \mathsf{P}_{\rm rad} = \frac{1}{3} \boldsymbol{\nabla} J. \tag{4.6}$$

we can rewrite Equation (4.5) as

$$-\kappa \rho \boldsymbol{F}_{\rm rad} = \frac{1}{3} \boldsymbol{\nabla} J. \tag{4.7}$$

Now, we can write $\boldsymbol{\nabla} \cdot \boldsymbol{F}_{\rm rad}$ as

$$\boldsymbol{\nabla} \cdot \left(\frac{1}{3\kappa\rho} \boldsymbol{\nabla} J \right) = -\boldsymbol{\nabla} \cdot \boldsymbol{F}_{\rm rad}, \tag{4.8}$$

$$\boldsymbol{\nabla} \cdot \left(\frac{1}{3\kappa\rho} \boldsymbol{\nabla} J \right) = 4\pi\kappa\rho \, (J - S) \tag{4.9}$$

$$\frac{1}{3} \left(\frac{1}{\kappa\rho} \boldsymbol{\nabla} \right)^2 J = 4\pi (J - S) \tag{4.10}$$

The thermostatic equilibrium can be satisfied if

$$\rho T \frac{\mathrm{D}s}{\mathrm{D}t} = 4\pi\kappa\rho(J - S) = 0. \tag{4.11}$$

If we substitute Equation (4.10) into Equation (4.11), we get

$$\left(\frac{1}{\kappa\rho}\boldsymbol{\nabla}\right)^2 J = 0. \tag{4.12}$$

Possible solutions are

1. $J = S \propto \tau$,
2. $J = S = \text{const}$.

In the optically thick part the first solution is obeyed and if we rewrite Equation (4.12) based on the source function $S = \sigma_{\mathrm{SB}}/\pi T^4$, we obtain exactly the diffusion approximation, where we have $K \cdot \boldsymbol{\nabla} T = \text{const}$. In all runs, K is smaller in the optically thick part than in the optically thin part. Therefore, we have larger $\boldsymbol{\nabla} T$ in the optically thick part than in the thin part. In all sets as we go from $\tilde{\kappa_0} = 10^4$ Mm^{-1} cm^3 g^{-1} to $\tilde{\kappa_0} = 10^7$ Mm^{-1} cm^3 g^{-1}, K decreases, so $\boldsymbol{\nabla} T$ increases and $\boldsymbol{\nabla} T$ levels off at smaller values of the temperature. In the optically thin part, the second solution is obeyed. There, κ decreases with height. Thus $1/\kappa$ becomes large in Equation (4.12). In order to maintain thermostatic equilibrium, $\boldsymbol{\nabla} J$ should be zero, which means J is constant. Therefore we obtain the isothermal solution for the optically thin part. In Figure 4.5, we plot outgoing intensity I^+ and incoming intensity I^- in the left panel and their corresponding temperature in the right panel for run A7 in the upper row and C7 in the lower one. The outgoing intensity I^+ is plotted in red and outgoing intensity I^- in blue. I^- decreases close to the upper boundary as we set $I^- = 0$ for incoming radiation. In our simulations, as explained in Section 3.3.1 the mean intensity is given by $J = (I^+ + I^-)/2$. As shown in Figure 4.5, I^+ is nearly constant in the optically thin part and I^- is small compared to I^+, so $\boldsymbol{\nabla} J \approx 0$. In the right panel of Figure 4.5, we plot the corresponding radiative flux in terms of the radiation temperature, which is given by

$$T^{\pm} = (\pi I^{\pm}/\sigma_{\mathrm{SB}})^{1/4}. \tag{4.13}$$

As we see in Figure 4.5, in the optically thick part, the corresponding temperatures of incoming and outgoing intensity lie nearly on top of each other. The difference between T^+ and T^- is constant, but it appears very small in the logarithmic representation. In the optically thin part, these two temperatures deviate from each other. The outgoing radiation temperature for both runs is constant, but slightly higher than the actual temperature. The incoming radiation temperature for both runs continues all the way to the boundary with the same gradient as in the optical thick part. The growth of I^- from zero is a consequence of the boundary condition, $I^- = 0$, at the top boundary, but the fact that the growth is linear near the top is a consequence of the difference $T - T^-$ being constant. In Figure 4.6, we plot I^+ and I^- in the non-logarithmic scale. The black lines in this figure represents the difference of I^+ and I^- in which $I^+ - I^- \approx 10^4$ erg cm^2 s^{-1} in the whole domain as we have radiative equilibrium $\boldsymbol{\nabla} \cdot \boldsymbol{F}_{\mathrm{rad}} = 0$. As a consequence, in the upper boundary the corresponding temperature of I^- is very low, and does not contribute as much as T^+. Therefore, the actual temperature has a small difference with T^+.

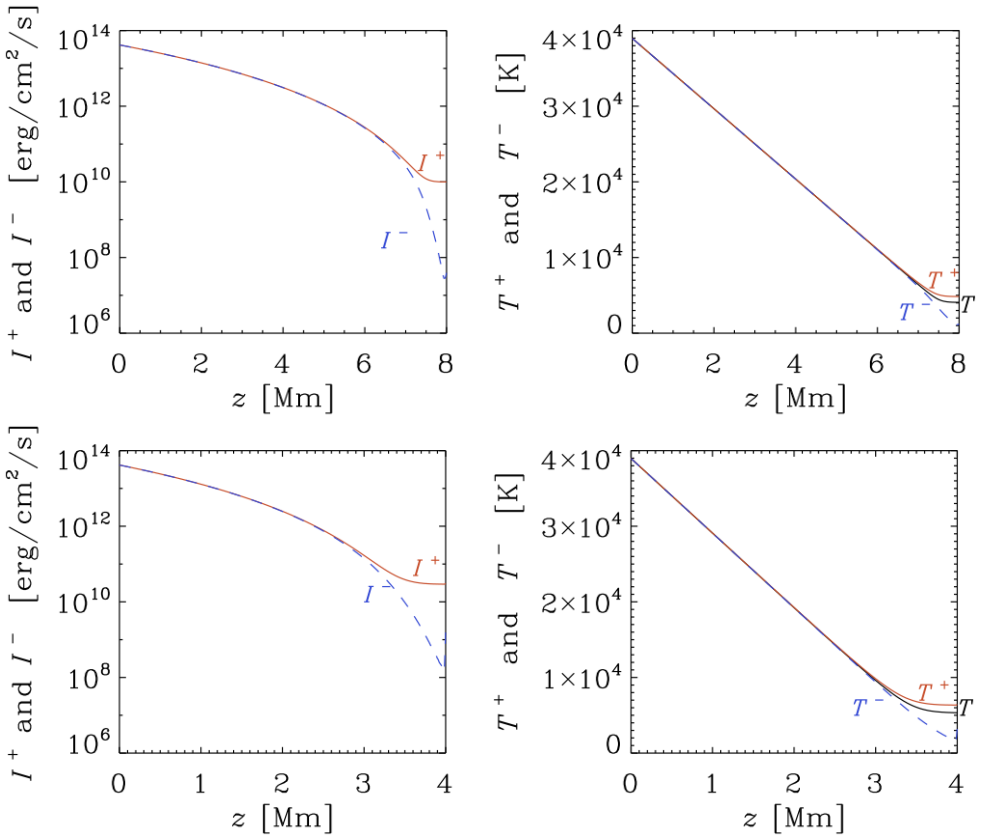

Figure 4.5: *Left panel*: Incoming intensity I^+ and outgoing intensity I^- over height for run A7 (upper panel) and run C7 (lower panel) with $\tilde{\kappa} = 10^7\ \mathrm{Mm}^{-1}\,\mathrm{cm}^3\,\mathrm{g}^{-1}$. The red line presents I^+ and dashed blue line represents I^-. *Right panel*: Corresponding temperature of incoming and outgoing intensity over height. Red lines represent the radiation temperature of incoming intensity T^+ and blue dashed lines that of out going intensity T^-. The black line shows the equilibrium temperature.

4.1.5 Radiative heat conductivity

In sets A, B, and C, the value of radiative heat conductivity K is constant in the optically thick part of the atmosphere, but not for set D. As we explained in Section 3.3.2, we expect to have a quasi-polytropic solution where radiative heat conductivity K is constant. $\boldsymbol{F}_{\mathrm{rad}}$ has a nonlinear dependency on both temperature and density, which makes the prediction of the result not straight forward. It was not clear in which part of the domain K will be constant, because if we substitute Equation (3.13) into Equation (3.5), we get

$$\boldsymbol{F}_{\mathrm{rad}} = -\frac{16\sigma_{\mathrm{SB}}T^{3-b}}{3\tilde{\kappa}_0\rho^2}\boldsymbol{\nabla}T. \tag{4.14}$$

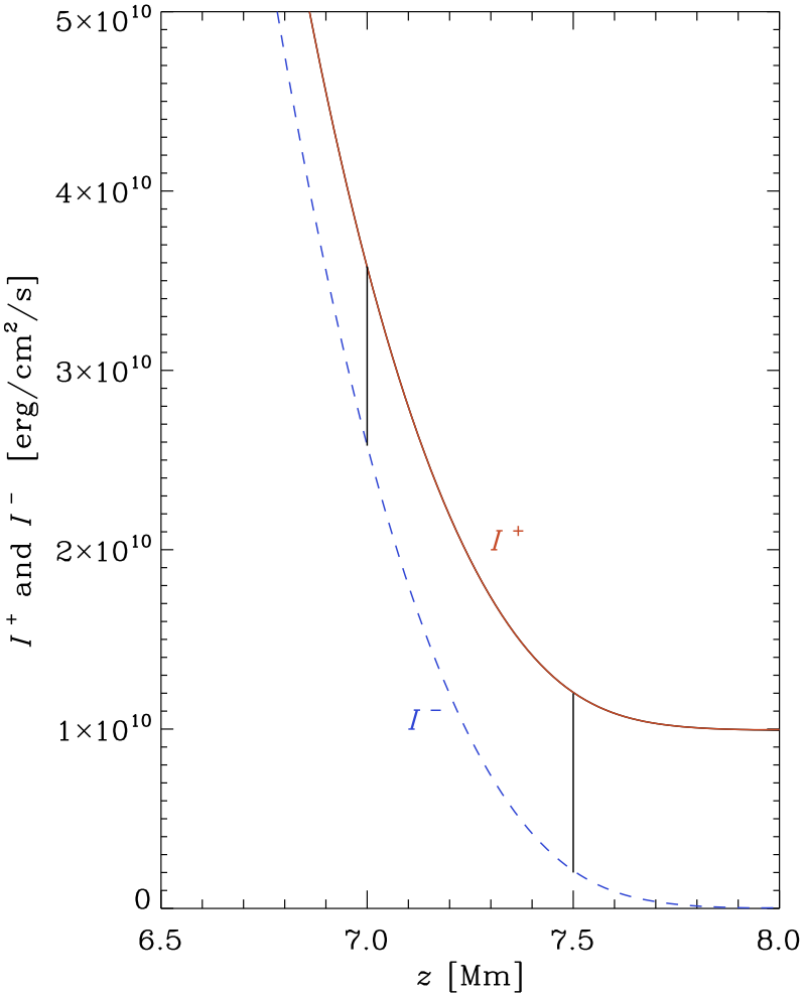

Figure 4.6: Incoming and outgoing intensity over height. The red line represents the incoming intensity I^+ and the blue line outgoing intensity I^- for run A7. The black vertical lines represent the difference of I^+ and I^-.

For different sets of runs, we have different values of b which means for each set we have

$$\boldsymbol{F}_{\text{rad}} \propto -\frac{T^{3-b}}{\rho^2}\boldsymbol{\nabla} T. \tag{4.15}$$

The value of K at the optically thick part of the domain is shown in Table 4.1 with K_{bot}. It has almost the same order of magnitude for A, B and C, independent of the value of b. But it is one order of magnitude larger for set D. This is due to the fact that in this set the density is lower in the optically thick part compared to the other sets. Moreover, as we go from higher values of $\tilde{\kappa_0}$ to the lower ones, the radiative heat conductivity increases. This can be explained by the inverse proportionality of K with opacity as $K \propto 1/\tilde{\kappa_0}$. For smaller value of $\tilde{\kappa_0}$, K is larger and vice versa. We plot the radiative heat conductivity

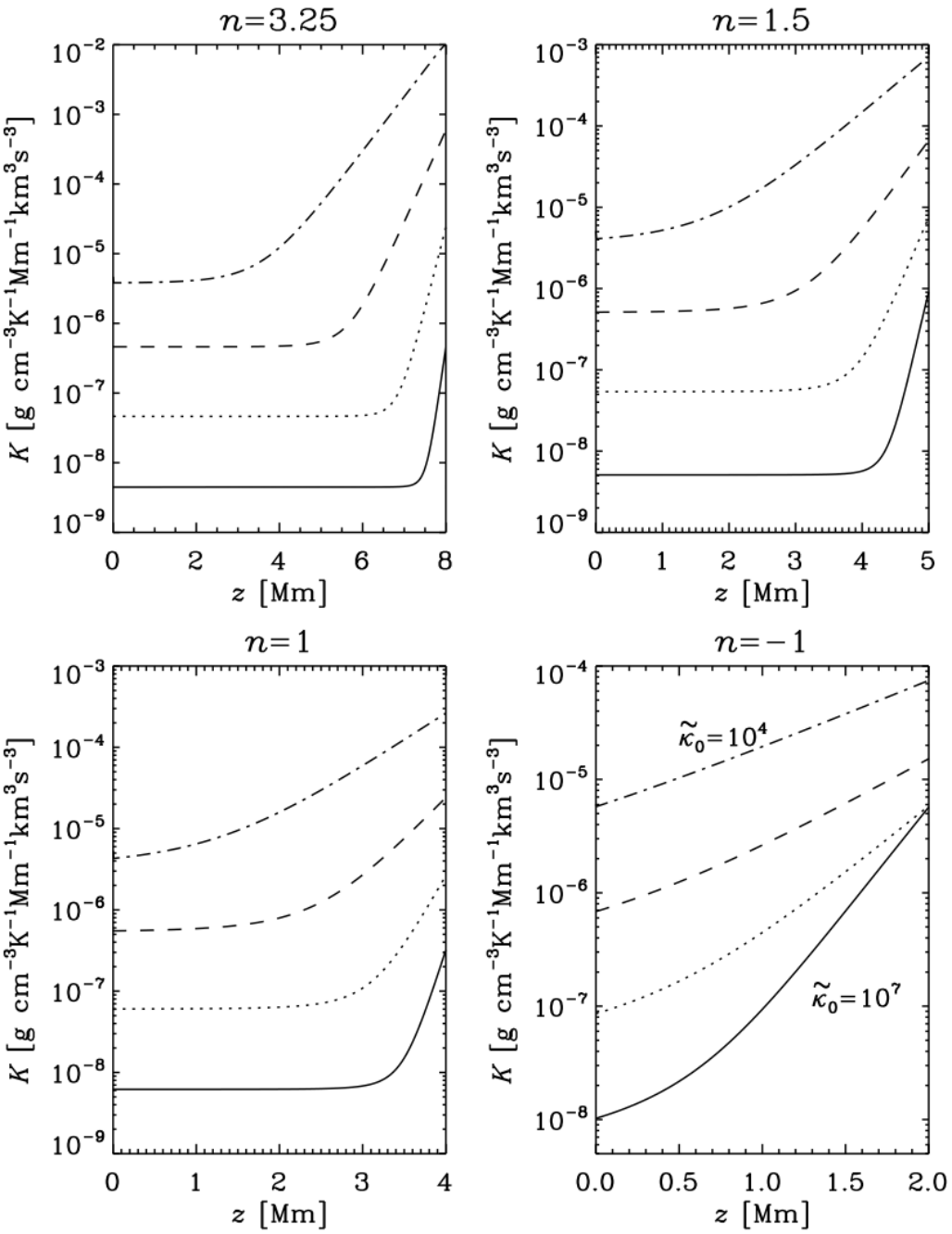

Figure 4.7: Radiative heat conductivity K over height for four sets of runs A (top left), B (top right), C (bottom left), and D (bottom right). In each plot K is plotted for different values of $\tilde{\kappa_0}$ where $\tilde{\kappa_0} = 10^4$ Mm^{-1} cm^3 g^{-1} is shown by dotted-dashed line, $\tilde{\kappa_0} = 10^5$ Mm^{-1} cm^3 g^{-1} dashed line, $\tilde{\kappa_0} = 10^6$ Mm^{-1} cm^3 g^{-1} dotted line and $\tilde{\kappa_0} = 10^7$ Mm^{-1} cm^3 g^{-1} solid line.

over height for all sets of runs in Figure 4.7. As we can see, K is constant in the optically

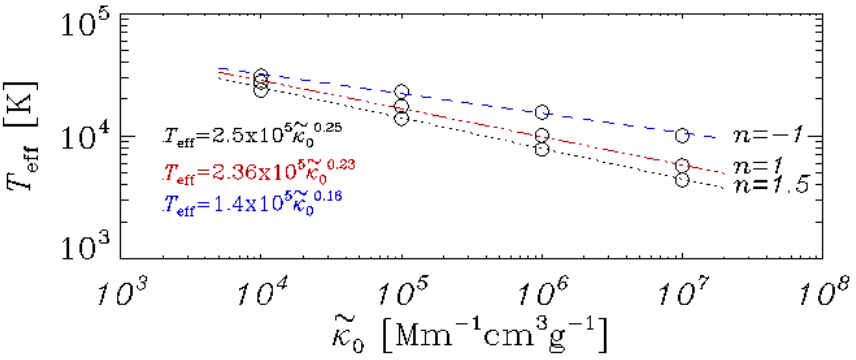

Figure 4.8: Effective temperature $T_{\rm eff}$ over height for four different sets A, B, C, and D. The circles show the numerical simulations. The dashed lines correspond to line fit of $T_{\rm eff}$ with normalized opacity $\tilde{\kappa_0}$

thick part and it starts to increase in the optically thin part. In the optically thin part, $\kappa\rho$ decreases, so K increases as $K \propto 1/\kappa$. To maintain $\boldsymbol{\nabla} \cdot \boldsymbol{F}_{\rm rad} = 0$, $\boldsymbol{\nabla} T$ has to decrease. As K increases even further, a thermostatic equilibrium can be satisfied if $\boldsymbol{\nabla} T$ comes close to zero.

4.1.6 Effective temperature

The effective temperature $T_{\rm eff}$ of all runs is calculated from the radiative flux $\boldsymbol{F}_{\rm rad}$,

$$T_{\rm eff} = \left(\frac{F_{\rm rad}}{\sigma_{\rm SB}} \right)^{1/4}. \tag{4.16}$$

$T_{\rm eff}$ of all sets of runs is summarized in Table 4.1. By increasing the value of b, $T_{\rm eff}$ also increases. The value of $T_{\rm eff}$ decreases as we go from lower to higher opacities for each set. For each sets of runs, we plot $T_{\rm eff}$ versus $\tilde{\kappa_0}$ in Figure 4.8. Circles represents the values of effective temperature for each set of runs for different values of $\tilde{\kappa_0}$. For each set of runs, we fit a line to $T_{\rm eff}$ versus $\tilde{\kappa_0}$. We find that $T_{\rm eff}$ has a power law relation with $\tilde{\kappa_0}$. The power of $\tilde{\kappa_0}$, which is the slope of the plot, depends on the polytropic index and therefore on b. For larger b the power is smaller than for smaller values of b. Additionally, the offset shows also a weak dependence on b. For the largest value, $b = 5$, $T_{\rm eff}$ is two times smaller than for the smallest value, $b = 0$. A power law relation between $T_{\rm eff}$ and the opacity of roughly 1/4 can be expected, because of the linear relation of the radiative flux and the opacity. For the larger of b, this dependency is no longer accurate. We also calculate for each run the corresponding optical depth where $T = T_{\rm eff}$. For all runs, $T_{\rm eff}$ corresponds to optical depth $\tau \approx 1/3$. This value is not the same as what theory predicts for a gray atmosphere, where $T_{\rm eff} = T$ at $\tau \approx 2/3$. This may be because in Equation (2.6.3), we cannot integrate all the way from ∞, but only from $z = z_{\rm top}$.

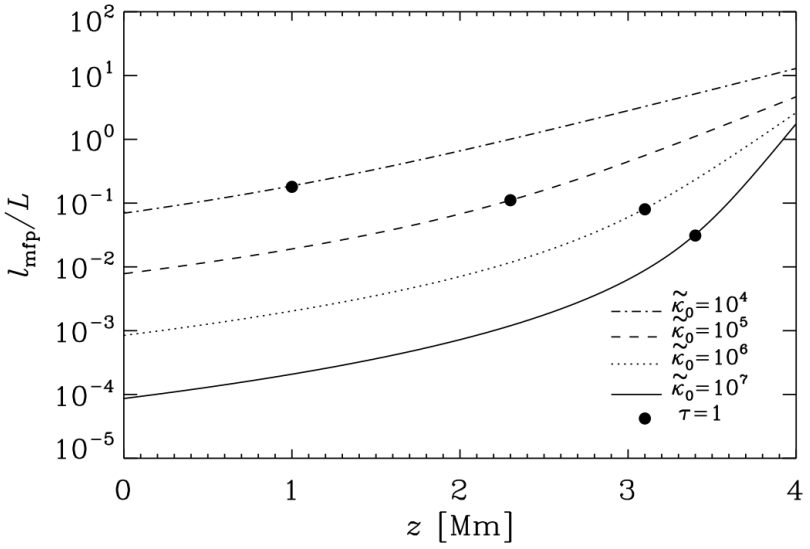

Figure 4.9: Normalized mean free path of photons $l_{\rm mfp}/L$ over height of run C7 with four different value of $\tilde{\kappa_0} = 10^4$, 10^5, 10^6, 10^7 $\mathrm{Mm^{-1}\,cm^3\,g^{-1}}$. The black dots represent the surface $\tau \approx 1$.

4.1.7 Thermal adjustment time

In our simulations we define a thermal adjustment time $\tau_{\rm adjust}$ which we define as the time it takes for each run to reach 1% of its final isothermal equilibrium temperature. The unit of $\tau_{\rm adjust}$ is ks. The value of $\tau_{\rm adjust}$ for all runs is summarized in Table 4.1. As we can see in Table 4.1, the thermal adjustment time becomes smaller for larger b and smaller n. For all sets of runs, $\tau_{\rm adjust}$ is smaller for smaller values of $\tilde{\kappa_0}$ and it increases as the opacity increases. But the dependency is not linear. As we increase $\tilde{\kappa_0}$ by an order of magnitude from 10^4 to 10^5, the adjustment time increases just by a factor of around 2 (sets A and C) or even less (sets B and D). Further increase of $\tilde{\kappa_0}$ shows an almost linear relation between $\tilde{\kappa_0}$ and $\tau_{\rm adjust}$. For larger values of $\tilde{\kappa_0}$, $\tau_{\rm adjust}$ seems to have a stronger dependency on b. We speculate that the reason for increasing the value of $\tau_{\rm adjust}$ for higher values of $\tilde{\kappa_0}$ is that by increasing the opacity the energy transport via radiation becomes less efficient as the mean free path of the photon decreases. But it seems that there exits a threshold of efficiency, leading to a larger adjustment time for the lowest values of $\tilde{\kappa_0}$, as expected. We plot over height the mean free path of the photons $l_{\rm mfp}$ normalized with the size of the domain L for set C for different value of $\tilde{\kappa_0}$. As we can see in Figure 4.9, the mean free path increases over several orders of magnitude from the bottom of the domain to the top. Furthermore, $l_{\rm mfp}$ is larger for smaller $\tilde{\kappa_0}$. In the optical thick part, the difference in $l_{\rm mfp}$ is one order of magnitude, which is equal to a corresponding change in $\tilde{\kappa_0}$. In the optical thin part, the difference of the values of $l_{\rm mfp}$ becomes smaller, as we reach the top of the domain. For $\tilde{\kappa_0} = 10^7$ $\mathrm{Mm^{-1}\,cm^3\,g^{-1}}$, $l_{\rm mfp}$ is the smallest one and it is three orders of magnitude smaller than for $\tilde{\kappa_0} = 10^4$ $\mathrm{Mm^{-1}\,cm^3\,g^{-1}}$. $l_{\rm mfp}$ is 10 times the size of the domain for $\tilde{\kappa_0} = 10^4$ $\mathrm{Mm^{-1}\,cm^3\,g^{-1}}$, which makes the cooling more efficient. We would

have expected to see a large change in the mean free path as we go through the surface. But the exponential growth seems to be roughly the same throughout the domain, at least for the smallest value of $\tilde{\kappa_0}$.

4.1.8 Properties of an atmosphere with undefined polytropic index

By choosing $a = -1$ and $b = 3$, we have a constant heat conductivity K which is not dependent on density and temperature as the heat conductivity is given by

$$K = \frac{16\sigma_{\rm SB}}{3\tilde{\kappa_0}}, \tag{4.17}$$

but the polytropic index n is given by

$$n = \frac{3-3}{1-1} = \frac{0}{0}. \tag{4.18}$$

In this case, we expect to have only a polytropic solution which satisfies the thermostatic equilibrium if $\nabla_z T = \text{const}$. We plot the profiles of temperature, density, and entropy profile of all the runs of set E in Figure 4.10. As expected, there is no isothermal part. The slope of temperature decreases approximately linearly as we go to higher values of $\tilde{\kappa_0}$, because K is related to the normalized opacity as $1/\tilde{\kappa_0}$. Although, we do not get any solution that has a transition from the polytropic part to the isothermal part, the atmosphere has a surface where $\tau = 1$ and it is shown with red dots in all panels of Figure 4.10. In contrast to the other sets, A, B, C, and D, the temperature profiles look qualitatively different. As in sets A, B, and C, in the optically thick part, the different temperature profiles have nearly the same gradient, while in set E, the gradient differ for different values of $\tilde{\kappa_0}$. This is due to the fact that the thermostatic equilibrium should be obeyed with the same constant K. In the second panel of Figure 4.10, the density profiles are almost the same for different values of $\tilde{\kappa_0}$ in the optically thick part and they decrease in the optically thin part. The density for higher values of $\tilde{\kappa_0}$ drops faster than in the case of smaller $\tilde{\kappa_0}$. In all cases, K is constant in both optically thick and thin parts, but the interesting thing is that its bottom value $K_{\rm bot}$ is of the same order of magnitude as in sets A, B, and C. In the third panel of Figure 4.10, we plot entropy profiles for the different values of $\tilde{\kappa_0}$. In all cases the entropy increases with a constant slope, which depends on $\tilde{\kappa_0}$. By plotting a versus b for different values of the polytropic index n, we see that all lines, which corresponds to different values of n intersect each other at $K = \text{const}$; see Figure 4.11. This means that the solution of constant K can belong to any of these polytropic indexes. As we explained in Section 2.5.1, in the absence of convection, all the energy is carried by radiation and we have $\nabla{=}\nabla_{\rm rad}$. We calculate the value of the polytropic index n using the superadiabatic gradient, which is given by

$$\Delta\nabla = \nabla - \nabla_{\rm ad} = \frac{{\rm d}s/c_{\rm p}}{{\rm d}\ln p}. \tag{4.19}$$

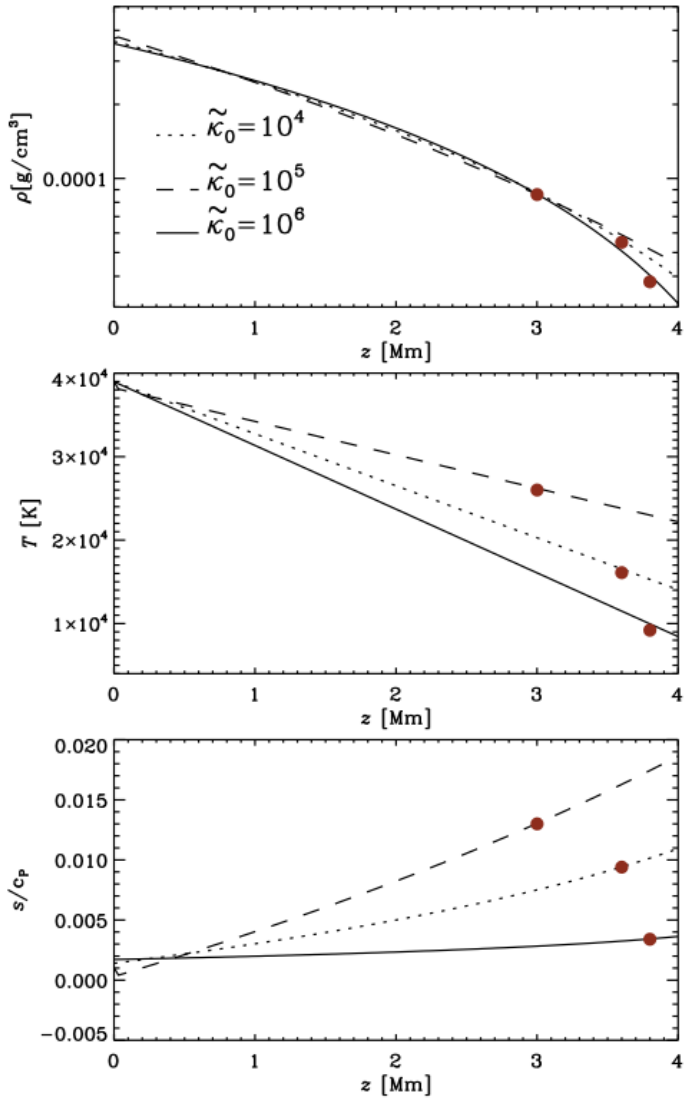

Figure 4.10: Temperature, density and entropy profile of $n = 0/0$ over height for three different values of $\tilde{\kappa_0} = 10^4, 10^5, 10^6$ $\mathrm{Mm}^{-1}\,\mathrm{cm}^3\,\mathrm{g}^{-1}$ for set E in the equilibrium state. The red dots present the surface of the model where $\tau = 1$.

We calculate the value of the polytropic index n using its definition in Equation (4.19) as the following

$$n = \frac{\mathrm{d}\ln\rho}{\mathrm{d}\ln T} \tag{4.20}$$

$$= \frac{\mathrm{d}\ln p}{\mathrm{d}\ln T} - \frac{\mathrm{d}\ln T}{\mathrm{d}\ln T} \tag{4.21}$$

$$= \frac{1}{\nabla} - 1. \tag{4.22}$$

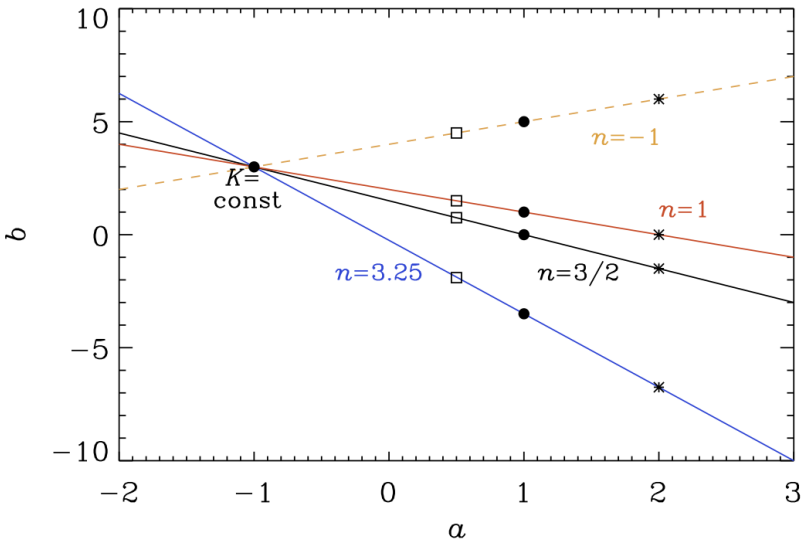

Figure 4.11: b versus a for different value of the polytropic index n. The black dots represents the combination of $a = 1$ with different values of b which are used in the main simulation; see Table 4.1. The stars represent the combination of $a = 2$ and squares represent $a = 0.5$ with different values of b; see Table 4.2.

We write Equation (4.19) in terms of ∇ and then substitute it into Equation (4.22), we get

$$n = \left(\nabla_{\rm ad} + \frac{{\rm d}s/c_{\rm p}}{{\rm d}\ln p} \right)^{-1} - 1. \tag{4.23}$$

Interestingly, this a priory undefined polytropic index turns out to be 3/2 which would be an isentropic radiative atmosphere. As we see, this is actually not quite the case as we see in the last panel of Figure 4.10, but the values of s are small.

4.1.9 Dependence on the size of the domain

The size of the domain plays an important role to get the polytropic and isothermal solutions for the temperature profile, as we have seen in sets A, B, C and D. The domain has to be big enough so the transition point lies inside the domain. In Figure 4.12, we show the temperature gradient over height for six different domain sizes for run A5. If the size of the domain is $z < 7\,{\rm Mm}$, it is too small to obtain the isothermal part where $\nabla_z T = 0$ and a boundary layer is produced. The reason that we cannot obtain the isothermal part can be explained by the initial density stratification which affect on opacity. In Figure 4.1, cutting the domain at different heights corresponds to a certain value of density at the upper part of the domain. This means that the opacity is not small enough to let the heat be radiated away. A size of around $z = 8\,{\rm Mm}$ is sufficient to get the isothermal part. However, a domain size which is too large ($z = 10\,{\rm Mm}$) leads to numerical difficulties near the top boundary. This is due to too low resolution in such a case. For all the runs shown in Table 4.1, we have always started by performing several test simulations to find a suitable domain size.

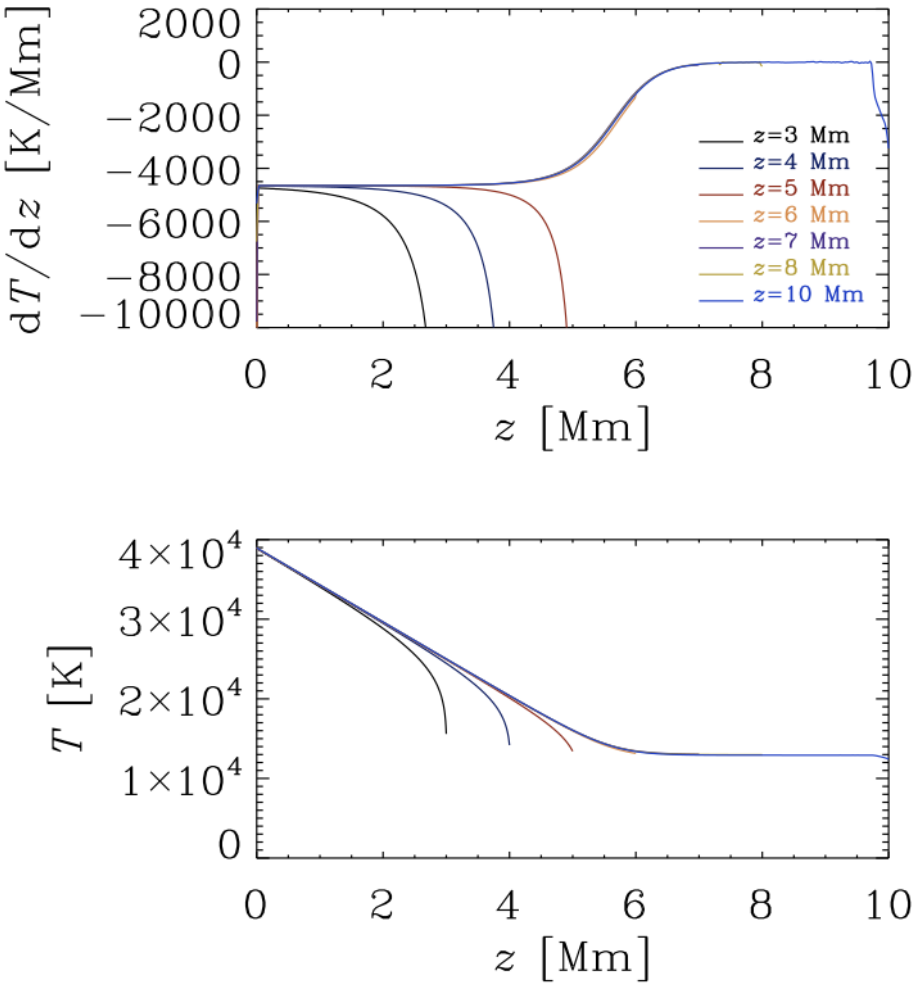

Figure 4.12: Gradient temperature (upper panel) and temperature profile (lower panel) of seven different sizes of the domain $z = 3, 4, 5, 6, 7, 8, 10$ Mm of run A5.

4.1.10 The same polytropic index with different a and b

As we can see in Figure 4.11, for a certain value of the polytropic index, we can choose different combinations of a and b. For each value of n that we have in Table 4.1, we choose two different other combinations of a and b. For example for the polytropic index $n = 1$ we choose two other combinations as $a = 0.5$ and $b = 1.5$ for one set and $a = 2$ and $b = 0$ for another one (see Table 4.2). We run eight more simulations with the same initial conditions as in previous runs and we obtain a similar equilibrium solution for the same polytropic index n. We calculate the effective temperature and the position where $\tau \approx 1$ as reference parameters with our old runs. The results are summarized in Table 4.2. For each set of runs with the same polytropic index, we labeled the runs similarly to those in Table 4.1. As we see in Table 4.2, for all the runs the effective temperature does not vary strongly,

Table 4.2: Summary of the result of different value of a and b with the same polytropic index n. $z_{\tau=1}$ is in the units of Mm and represents the position where $\tau \approx 1$. $T_{\rm eff}$ is the effective temperature.

Run	a	b	n	$z_{\tau=1}$	$T_{\rm eff}$
F1	0.5	-1.9	3.25	5.3	13,906
F2	1	-3.5	3.25	5.2	13,900
F3	2	-6.75	3.25	5.1	13,998
G1	0.5	0.75	1.5	3.2	16,603
G2	1	0	1.5	2.9	16,304
G3	2	-1.5	1.5	2.7	16,089
H1	0.5	1.5	1	2.6	17,089
H2	1	1	1	2.3	17,468
H3	2	0	1	2.1	18,021
I1	0.5	4.5	-1	1.1	21,809
I2	1	5	-1	0.8	23,118
I3	2	6	-1	0.6	23,718

but there is a systematic behavior. By increasing the value of a, the effective temperature increases and the surface is shifted to the lower part of the domain. By increasing the exponent of the density, the opacity increases. As a consequence, the mean free path of the photons increases. Hence, the atmosphere reaches its equilibrium at a higher value of effective temperature (see Section 4.1.4). The stratification of temperature and other important properties of these atmospheres can be explained analogously to runs A, B, C and D.

4.1.11 Numerical stability

In numerical simulations, the thermal diffusivity χ is an important parameter, just like the viscosity. These numbers determine whether the results of numerical turbulence simulations are reliable or not and whether they are able to dissipate all the energy within the mesh. In a numerical simulation we are restricted to a certain number of grid points. If the diffusion of the temperature in a simulation is very small, it can happen that the changes in the temperature are too large over the distance of neighboring grid points. Hence, the changes of the temperature cannot be resolved in such a simulations. Therefore, it is important to measure how large are the thermal diffusivity in our models of a radiative atmosphere. The Péclet number is a dimensionless number that quantifies the importance of advective and

diffusive term, which is here defined as

$$\mathrm{Pe} = u_{\mathrm{rms}} H_{\mathrm{p}} / \chi, \tag{4.24}$$

where H_{p} is a pressure scale height and u_{rms} is rms velocity. The radiative diffusivity is defined as

$$\chi = K / c_{\mathrm{p}} \rho, \tag{4.25}$$

where K is radiative heat conductivity. As we do not solve for a velocity equation in our model, so we use instead the sound speed, which can be related to u_{rms} via the Mach number $\mathrm{Ma} = u_{\mathrm{rms}}/c_{\mathrm{s}}$. The normalized Péclet number in our simulation $\widetilde{\mathrm{Pe}}$ is then given by

$$\widetilde{\mathrm{Pe}} \equiv \mathrm{Pe}/\mathrm{Ma} = c_{\mathrm{s}} H_{\mathrm{p}} / \chi. \tag{4.26}$$

We plot $\widetilde{\mathrm{Pe}}$ for all sets of runs in Figure 4.4. As we can see for all sets of runs, $\widetilde{\mathrm{Pe}}$ is a large number for the optically thick part and it decreases as we go toward the optically thin part. This can be explained with Equation (4.25), where χ is proportional to K. In the optically thin part, K increases, so χ increases. As a result, $\widetilde{\mathrm{Pe}}$ decreases. $\widetilde{\mathrm{Pe}}$ is also larger for the larger value of $\tilde{\kappa_0}$.

4.2 Preliminary results on the turbulent magneto-thermal instability

The one-dimensional results presented above are essential steps toward constructing a model of what is called the magneto-thermal instability. Initial exploratory simulations suggested that radiation may have a detrimental effect on the development of this instability. Although this is not yet well understood, we give here some preliminary results that illustrate the ultimate goal.

In the following, we use turbulent values of the fluid and magnetic Prandtl numbers, defined here as $\mathrm{Pr_t} = \nu_{\mathrm{t}}/\chi_{\mathrm{t}}$ and $\mathrm{Pr_{Mt}} = \nu_{\mathrm{t}}/\eta_t$, respectively. We choose unity for those values and vary the value of ν_{t} ($= \chi_{\mathrm{t}} = \eta_t$) such that we are close to the onset of mean-field convection, so there should not be any convective motions as in the mean-field the average of the up-flow and down-flow average each other out. This value turned out to be close to $\nu_{\mathrm{t}} = 4\,\mathrm{Mm\,km/s}$, corresponding to $4 \times 10^{13}\,\mathrm{cm^2\,s^{-1}}$. The value of $\widetilde{\mathrm{Ra}}$ is then around 100. This can be explained according to the value of the kinetic energy which is defined as $E_{\mathrm{kin}} = \int \frac{1}{2} \overline{\rho} \overline{\boldsymbol{U}}^2$ and its time derivative. As we can see in the fourth row of Table 4.3, the value of $\dot{E}_{\mathrm{kin}}$ becomes negative, which means it is decreasing with time. It turned out to be difficult to find a perfect equilibrium, so we quote in Table 4.3 the resulting values of kinetic energy, E_{kin}, its time derivative $\dot{E}_{\mathrm{kin}}$, the rms value of macroscopic velocity and magnetic field, $\overline{U}_{\mathrm{rms}}$ and $\overline{B}_{\mathrm{rms}}$, respectively, and the mean and maximum values of $\beta = |\overline{B}|/B_{\mathrm{eq}}$ at $\tau = 1$, which is around $z \approx 3\,\mathrm{Mm}$. We also vary the value of the imposed field B_0 in the range from 1–100 G. The results are given in Table 4.3 and a visualization of the flow and the resulting magnetic field and entropy are shown in Figure 4.13. It turns out that $\beta_{\mathrm{max}}/\langle\beta\rangle$ is only around 2.3. We expect this value to become bigger if there is structure formation due to the turbulent thermo-magnetic instability, but this does not seem to be the case.

Table 4.3: Summary of models showing that the convectively marginal case is achieved near $\nu_t \approx 3\,\mathrm{Mm\,km\,s^{-1}}$. Here, B_0 is in G, ν_t is in $10^{13}\,\mathrm{cm^2\,s^{-1}}$ ($=\mathrm{Mm\,km\,s^{-1}}$), and $t_{\rm end}$ is the run time in ks. $\beta = B/\sqrt{\mu_0\overline{\rho}}u_{\rm rms}$ is dimensionless, and the ratio between maximum and average values is around 2.5 in all cases, suggesting that no flux concentrations occur. The ratio between $\beta_{\rm max}$ and $\langle\beta\rangle$ is expected to increase if there are flux concentrations, but this is not the case.

B_0	ν_t	Ra	$E_{\rm kin}$	$\dot{E}_{\rm kin}$	$\overline{U}_{\rm rms}$	$\overline{B}_{\rm rms}$	$\langle\beta\rangle$	$\beta_{\rm max}$	$t_{\rm end}$
5	2.0	422	5.730	1.23	2.894	2.510	0.053	0.103	12.36
20	2.0	446	3.100	4.49	1.832	6.800	0.173	0.413	12.27
100	3.0	187	0.206	0.12	0.539	9.310	0.212	0.440	12.30
100	4.0	105	0.078	−0.00	0.352	5.760	0.124	0.276	12.37
100	4.0	105	0.078	−0.00	0.352	5.770	0.125	0.276	12.38
100	4.0	105	0.078	−0.00	0.352	5.780	0.125	0.277	12.39
1	5.0	67	0.037	−0.02	0.253	0.040	0.001	0.002	12.23
1	5.0	67	0.037	−0.02	0.254	0.040	0.001	0.002	12.23
1	5.0	67	0.043	−0.02	0.274	0.040	0.001	0.002	12.17
1	5.0	67	0.043	−0.02	0.274	0.040	0.001	0.002	12.17
5	5.0	67	0.047	−0.03	0.284	0.210	0.004	0.010	11.95
20	5.0	67	0.035	−0.02	0.247	0.770	0.016	0.036	12.32
100	5.0	67	0.034	−0.02	0.240	3.680	0.079	0.175	12.39

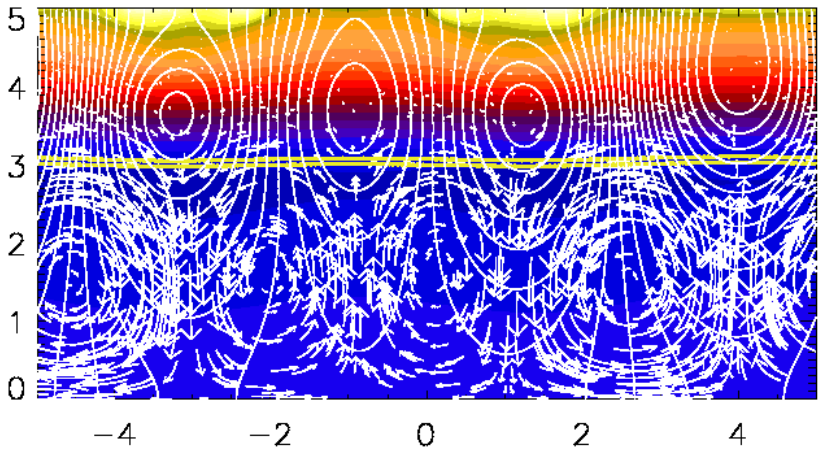

Figure 4.13: Flow and field structure for a run with $\nu_t = 5\,\mathrm{Mm\,km/s}$ and $B_0 = 100\,\mathrm{G}$ showing specific entropy color coded together with contours of $\overline{B}_y$ together with streak lines of the mass flow $\overline{\rho}\overline{\boldsymbol{U}}$ in white. The $\tau = 2/3$ and $\tau = 1$ lines are shown in yellow.

Chapter 5

Discussions and conclusions

In preparation for two–dimensional hydromagnetic mean-field calculations of the Sun's surface layers, we have computed models of gray radiative atmospheres using the Pencil Code with generalized Kramers opacity. To isolate the effects of radiation from those of partial ionization, we have assumed that the atmosphere is completely ionized and in LTE. We have performed five sets of simulations by changing the dependency of the opacity on the power of temperature which corresponds to different polytropic atmosphere. For each set, we run four simulations with different prefactor in the generalized Kramers opacity law. In all sets, except for the model with undefined polytropic index, we obtain a polytropic atmosphere in the lower part of the domain and an isothermal atmosphere in the upper part of the domain. The transition point coincides with the surface $\tau \approx 1$.

Increasing the prefactor in the generalized Kramers opacity law corresponds to lowering the radiative conductivity in the optically thick part of the domain, and hence to lower fluxes and lower effective temperatures. The physical values of this prefactor are much larger than those used here, but larger prefactors lead to values of the radiative diffusivity that become eventually so small that temperature fluctuations on the mesh scale cannot be dissipated by radiative diffusion. In all previous work (Nordlund, 1982; Steffen et al., 1989; Vögler et al., 2005; Heinemann et al., 2006, 2007; Rempel, 2011), this problem has been avoided by applying numerical diffusion or using numerical schemes that dissipate the energy when needed. However, this may also suppress the possibility of physical instabilities that we are ultimately interested in. This motivates the investigation of models with prefactors in the Kramers opacity law that are manageable without the use of numerical procedures to dissipate energy artificially.

As initial condition, one normally uses a vertical background stratification that has been obtained earlier by integrating a stellar envelope model. It turns out that this is not actually necessary. Instead, we have here been able to start from an isothermal stratification. Such an initial condition satisfies hydrostatic equilibrium, but it is obviously not in thermal equilibrium. As long as the aforementioned prefactor in the Kramers opacity law is not too large, the final equilibrium state is reached in a relatively short amount of time. However, as this prefactor is increased further, the relaxation time can become prohibitively long.

It turns out that in all cases with a and b such that $n > -1$, the stratification corresponds to a polytrope below the photosphere and to an isothermal one above it. This was actually expected given that such a solution has previously been obtained analytically in the special case of constant κ (corresponding to $a = b = 0$); see Spiegel (2008). On the other hand, the isothermal part was apparently not present in the simulations of Edwards (1990).

As the prefactor of the opacity $\tilde{\kappa_0}$ contain the metallicity inherently, we can also naively

interpret it as the metallicity of the atmosphere. By increasing the value of $\tilde{\kappa_0}$ one order of magnitude in each sets of runs, we increase the metallicity which leads to more absorption of the radiation field and decreasing the radiative flux.

As we change the value of κ_0, we find that $T_{\rm eff}$ changes inversely proportional to κ_0 when $n = 3/2$, but this dependence becomes slightly shallower both for $n = 1$ and $n = -1$. We also find that in a domain that is less tall, the solution is basically unchanged as long as the top boundary happens to be within the optically thin part. Otherwise, if the height of the domain is reduced further, such that the top boundary lies within the optically thick part, a narrow boundary layer develops, in which the vertical gradient becomes very steep. This is just the opposite trend of what one obtains in a tall domain. The prefactor $\tilde{\kappa_0}$ not only plays role to determine the temperature and density stratification, but it also can play an important role to make an atmosphere convectively unstable or not. In set D, we expect to have negative gradient of entropy according to the Schwarzschild criteria, but for the value of $\tilde{\kappa_0} = 10^4\ \mathrm{Mm^{-1}\,cm^3\,g^{-1}}$, we do not obtain an atmosphere which is convectively unstable.

Our ultimate goal is to investigate solar surface phenomena. Therefore it is important to have at least a temperature profile close to the solar surface. Just below the surface of the Sun, there is big jump in the temperature profile where the temperature decreases by two orders of magnitude. On the other hand, in our simulations there is no jump in the temperature profile about the surface and it changes smoothly from the polytropic to the isothermal part. We suspect that he reason for this difference is that the radiative atmosphere is completely ionized, but in the atmosphere of the Sun, hydrogen is partially ionized. In the Sun, the density from the upper part of the convection zone decreases by two orders of magnitude as we go to the photosphere. This makes the opacity smaller and the atmosphere in the photosphere becomes transparent. Therefore photons can be radiated away. As the temperature cools down, there is not enough energy to ionize hydrogen. As a consequence, the number of electrons also decreases. As is well known, the ionization energy of H^- is 0.75 eV which corresponds to temperatures in the range $4000\,\mathrm{K} < T < 7000\,\mathrm{K}$. At the height where this temperature is reached, the H^- opacity becomes important, which is not included in our simulations. This lower temperature leads to a decrease of the number of electrons, because the hydrogen becomes neutral at these temperatures. The radiative heat conductivity in our simulations is found to be constant throughout the optically thick part, whereas it increases in the optically thin part. One might think that, as radiative heat conductivity has a reciprocal relation with opacity, or better optical depth, as we go from the surface deeper down in the atmosphere, we expect that heat conductivity decreases. But, according to our result radiative heat conductivity stays constant in the optically thick part, independently of the sensitivity of the opacity on the temperature.

As we see in our 2D simulation, interpreting the result is not trivial, because we have not studied the radiative surface in two-dimensional case. Especially, studying the magneto-thermal instability which is directly related to the suppression of the convective heat flux, knowing the properties of the heat transport with radiation can be crucial. For example, thermal adjustment time can be different from 1D simulations as we have 8 rays to carry the radiation instead of two rays. This can be an important affect. In our 2D simulation we choose $\tilde{\kappa_0} = 10^2$ and we obtained a surface at height $z = 3$, but we saw that in the 1D simulation we could not obtain the radiative surface as this factor makes the medium

not optically thick enough to have even a radiative surface. We know that in reality the radiative surface of a star is not one- dimensional. It is a three dimensional time dependent phenomena. For example, granules, sunspots and speckles are all solar surface properties.

Especially, important phenomena which cannot be studied in 1D simulations and cannot be ignored is the convection in the stellar surface. Convection is a time-dependent, non-local and turbulent phenomena (Magic et al., 2013). At the surface, the interaction of the radiative flux and convective flux can be important fact that determine the temperature stratification of a star. As it is shown in the work by Brandenburg et al. (2005), for different values of a and b which corresponds to a polytropic index n, the ratio of a radiative flux to convective flux can be changed and when the radiative flux becomes important, the properties of the convection can depend on this radiative flux. As our 2D runs are not in a mature state, we cannot judge the result that is obtained by Kitchatinov & Mazur (2000). we assume that $\nu_{\rm t}$ and η_t are constant in our simulation, but in the work by Kitchatinov & Mazur (2000), these two parameters are also modeled a magnetic field dependent. We only implement a magnetic dependent turbulent heat diffusivity $\chi_{\rm t}$ in the Pencil Code. How this will influence the results need more detailed studies of a set of simulations

Another important thing that should be mentioned is that in the mean-field model the correlation of fluctuating quantities expressed in terms of mean-field quantities. The effect of the including radiative transfer equation in the mean field model is not fully understood yet. Maybe there are some correlation that can play an important role that is not included in the equations yet.

In summary, in this thesis, we perform a 1D model of radiative atmosphere, which result in having a one-dimensional domain containing a radiative surface within the domain assuming LTE and gray atmosphere, using Kramers opacity. We show that for different polytropic atmospheres with different combination of a and b which can leads to a certain polytropic index n, we can use an adjustable parameter $\tilde{\kappa_0}$ that can leads to a certain effective temperature in this radiative atmosphere. However, the value of $\tilde{\kappa_0}$ is six order of magnitude smaller than physical value in the Kramers opacity law in the bound-free transition. In principal, we can increase the value of the adjustable parameter $\tilde{\kappa_0}$, but this option leads to a large Péclet number which makes a numerical simulation not feasible. In addition the thermal adjustment time will increase drastically by increasing this adjustable parameter. We also interestingly find that the radiative heat conductivity is constant in the optically thick part of the domain and it starts increasing as we go to the optically thin part of the domain. Moreover, we see that in the radiative atmosphere model which is completely ionized, rather than partially ionized, the temperature profile does not have a sharp drop of the temperature near the surface and the temperature becomes nearly constant close to the surface.

The main simplification in our simulation is that we assume that the LTE holds in our atmosphere. As we are interested in having an atmosphere which is few Mm below and above the surface, the LTE can be hold. In these depth the density is high enough that we can assume that the collisions between particles can hold the Maxwell-Boltzmann distribution of the level populations.

Another important thing in our simulation is that we assume gray approximation. In this approximation the opacity does not depend on the frequency. But in reality the opacity is a highly frequency-dependent parameter. In order to have a realistic model of

the temperature stratification of the atmosphere of stars, it is necessary to include spectral lines that are important in the certain height in the atmosphere. This can have an important effect on the temperature stratification.

In this work we mainly focus on 1D simulations to better understand the effect of radiative cooling in the stratification of the atmosphere but as a preliminary test, we see that this 1D model can be also extended to 2D. We can conclude that the radiative transfer in the surface phenomena can play an important role as it affects the temperature and density stratification. It will be interesting to extend this work to 2D simulations, and investigate all the physical parameter, specially in the case that we also have convective motion which contribute to the energy transport. We also interested in including partial ionization to the 1D atmosphere to see the affect of the ionization in the temperature profile. In this work we use a gray atmosphere, it also worth to do the same setup for a frequency dependent opacity, and see how it can affect the density stratification close to the surface.

APPENDIX

Table 5.1: Summary of some universal constants used in the thesis.

parameter	amount	unit
Stefan–Boltzmann constant	$\sigma_{\rm SB}= 5.670400 \times 10^{-5}$	$\mathrm{erg\,cm^{-2}\,s^{-1}\,K^{-4}}$
Boltzmann constant	$k_{\rm B} = 1.3806505 \times 10^{-16}$	$\mathrm{erg\ K^{-1}}$
radiation constant	$a = 7.5657 \times 10^{-15}$	$\mathrm{erg\,cm^{-3}\,K^{-4}}$
light speed	$c = 2.99792458 \times 10^{10}$	$\mathrm{cm\,s^{-1}}$
gas constant	$R = 8.3144 \times 10^{7}$	$\mathrm{erg\,K^{-1}\,mol^{-1}}$

Bibliography

Babkovskaia, N. ; Haugen, N. E. L. ; Brandenburg, A.: A high-order public domain code for direct numerical simulations of turbulent combustion. In: *Journal of Computational Physics* 230 (2011), S. 1–12

Bohm-Vitense, E. ; Trimble, V.: Book-Review - Introduction to Stellar Astrophysics - V.2 - Stellar Atmospheres. In: *Comments on Astrophysics* 16 (1993), S. 278

Brandenburg, A. ; Chan, K. L. ; Nordlund, Å. ; Stein, R. F.: Effect of the radiative background flux in convection. In: *Astronomische Nachrichten* 326 (2005), S. 681–692

Brandenburg, A. ; Dobler, W.: Hydromagnetic turbulence in computer simulations. In: *Computer Physics Communications* 147 (2002), S. 471–475

Brandenburg, A. ; Subramanian, K.: Astrophysical magnetic fieds and nonlinear dynamo theory. In: *Physics Reports* 417 (2005), S. 1–209

Charbonneau, P.: Solar and Stellar Dynamos. In: *Society for Astronomical Sciences Annual Symposium* 39 (2013)

Clarke, C. ; Carswell, B.: *Principles of Astrophysical Fluid Dynamics*. 2007

Edwards, J. M.: Two-dimensional radiative convection in the Eddington approximation. In: *MNRAS* 242 (1990), S. 224–234

Feautrier, P.: A Procedure for computing the Mean Intensity and the Flux. In: *SAO Special Report* 167 (1964), S. 80

Gudiksen, B. ; Nordlund, Å.: An ab initio approach to the solar coronal heating problem. In: *ApJ* 618 (2005), S. 1020–1030

Hale, G. E.: On the Probable Existence of a Magnetic Field in Sun-Spots. In: *ApJ* 28 (1908), S. 315

Heinemann, T. ; Dobler, W. ; Nordlund, Å. ; Brandenburg, A.: Radiative transfer in decomposed domains. In: *A&A* 448 (2006), S. 731–737

Heinemann, T. ; Nordlund, Å. ; Scharmer, G. B. ; Spruit, H. C.: MHD Simulations of Penumbra Fine Structure. In: *ApJ* 669 (2007), S. 1390–1394

Johansen, A. ; Oishi, J. S. ; Mac Low, M.-M. ; Klahr, H. ; Henning, T. ; Youdin, A.: Rapid planetesimal formation in turbulent circumstellar disks. In: *Nature* 448 (2007), S. 1022–1025

Käpylä, P. J. ; Mantere, M. J. ; Brandenburg, A.: Cyclic Magnetic Activity due to Turbulent Convection in Spherical Wedge Geometry. In: *ApJ* 755 (2012), S. L22

Kemel, K. ; Brandenburg, A. ; Kleeorin, N. ; Mitra, D. ; Rogachevskii, I.: Active Region Formation through the Negative Effective Magnetic Pressure Instability. In: *Sol. Phys.* (2012)

Kitchatinov, L. L. ; Mazur, M. V.: Stability and equilibrium of emerged magnetic flux. In: *Sol. Phys.* 191 (2000), S. 325–340

Kunasz, P. ; Auer, L. H.: Short characteristic integration of radiative transfer problems - Formal solution in two-dimensional slabs. In: *J. Quant. Spec. Radiat. Transf.* 39 (1988), S. 67–79

Magic, Z. ; Collet, R. ; Asplund, M. ; Trampedach, R. ; Hayek, W. ; Chiavassa, A. ; Stein, R. F. ; Nordlund, Å.: The Stagger-grid: A Grid of 3D Stellar Atmosphere Models - I. Methods and General Properties. In: *ArXiv e-prints* (2013)

Nordlund, A.: Numerical simulations of the solar granulation. I - Basic equations and methods. In: *A&A* 107 (1982), S. 1–10

Nordlund, Å. ; Stein, R. F. ; Asplund, M.: Solar Surface Convection. In: *Living Reviews in Solar Physics* 6 (2009), S. 2

Rempel, M.: Subsurface Magnetic Field and Flow Structure of Simulated Sunspots. In: *ApJ* 740 (2011), S. 15

Rutten, R. J.: *Radiative Transfer in Stellar Atmospheres.* 2003

Schuessler, M.: Flux tube dynamo approach to the solar cycle. In: *Nature* 288 (1980), S. 150–152

Spiegel, E. A.: An Introduction to Radiative Transfer for Geophysicists. 744 (2008), S. 85

Steffen, M. ; Ludwig, H.-G. ; Kruess, A.: A numerical simulation study of solar granular convection in cells of different horizontal dimension. In: *A&A* 213 (1989), S. 371–382

Stein, R. ; Nordlund, A.: Spontaneous Pore Formation in Magneto-Convection Simulations. In: Golub, L. (Hrsg.) ; De Moortel, I. (Hrsg.) ; Shimizu, T. (Hrsg.): *Fifth Hinode Science Meeting* Bd. 456, 2012 (Astronomical Society of the Pacific Conference Series), S. 39

Stein, R. F. ; Nordlund, A.: Simulations of Solar Granulation. I. General Properties. In: *ApJ* 499 (1998), S. 914

Stix, M.: *The Sun. An introduction.* Springer, Berlin, 1989

Vögler, A. ; Shelyag, S. ; Schüssler, M. ; Cattaneo, F. ; Emonet, T. ; Linde, T.: Simulations of magneto-convection in the solar photosphere. Equations, methods, and results of the MURaM code. In: *A&A* 429 (2005), S. 335–351

Warnecke, J. ; Brandenburg, A. ; Mitra, D.: Dynamo-driven plasmoid ejections above a spherical surface. In: *A&A* 534 (2011), S. A11